Proof Central

Dear Author

Please use this PDF proof to check the layout of your article. If you would like any changes to be made to the layout, you can leave instructions in the online proofing interface. First, return to the online proofing interface by clicking "Edit" at the top page, then insert a Comment in the relevant location. Making your changes directly in the online proofing interface is the quickest, easiest way to correct and submit your proof.

Please note that changes made to the article in the online proofing interface will be added to the article before publication, but are not reflected in this PDF proof.

If you would prefer to submit your corrections by annotating the PDF proof,
please download and submit an annotatable PDF proof by clicking the link below.

Annotate PDF

Materials Today • Volume xxx, Number xx • xxxx 2025

Advances and perspectives of hard carbon anode modulated by defect/hetero elemental engineering for sodium ion batteries

Haihan Zhang [a], **Siyuan Lin** [a], **Chengyong Shu** [a,⁎], **Zexun Tang** [d], **Xiaowei Wang** [c,⁎], **Yuping Wu** [e,⁎], **Wei Tang** [a,b,⁎]

[a] School of Chemical Engineering and Technology, Xi'an Jiaotong University, Xi'an 710049, China
[b] National Innovation Platform (Center) for Industry-Education Integration of Energy Storage Technology, Xi'an Jiaotong University, Xi'an 710049, China
[c] Chemical Sciences and Engineering Division, Argonne National Laboratory, Lemont, IL 60439, USA
[d] College of Materials and Chemical Engineering, Hunan Institute of Engineering, Xiangtan 411104, China
[e] School of Energy and Environment, Southeast University, Nanjing 210096, China

Sodium-ion batteries (SIBs) serve as a promising complement to lithium-ion batteries for large-scale energy storage, leveraging the abundance of sodium resources and notable safety advantages. The key advancement in SIB industrialization hinges on identifying a cost-effective and high-performance anode material, similar to the graphite anode in lithium-ion batteries. Hard carbon emerges as prime anode materials for SIBs, boasting high specific capacity, low sodium storage potential, and wide availability. However, practical applications of hard carbon encounters challenges such as low initial Coulombic efficiency (ICE), inadequate long-term cycling stability, and poor rate performance. Recent research has focused on the optimization of hard carbon electrodes through functional design. In this comprehensive review, we have meticulously examined the progress in enhancing sodium storage performance through microstructural modulation within hard carbon, encompassing four pivotal aspects: heteroatom doping, incorporation of oxygen functional groups, surface coating, and intrinsic defect engineering. Progress in implementing these strategies is scrutinized, while the merits and challenges of each defect engineering approach are discussed. This review also looks into forthcoming opportunities and challenges in the practical application process of hard carbon electrodes in SIBs.

Keywords: Hard carbon anode; Defect engineering; Structural modulation; Practical applications; Sodium-ion batteries

Introduction

As the issue of energy depletion caused by the excessive exploitation of fossil fuels grows increasingly severe, the development and utilization of renewable energy have become crucial measures for low-carbon and clean transformation of the energy sector, ensuring energy security [1–3]. However, renewable energy such as solar, wind, and hydropower often pose challenges due to their unstable supply, when integrated directly into the power grid [4,5]. Driven by this, emerging energy storage technologies, particularly electrochemical storage, offer reliable solutions for the large-scale integration of renewable energy into the grid [6,7].

Lithium-ion batteries (LIBs), renowned for their high energy density and long cycle life, have gained extensive attraction in energy market, notably dominating the power sector. Sodium, sharing similar chemical properties with lithium, holds promise as an alternative [8–10]. While sodium-ion batteries (SIBs) exhibit a lower energy density than LIBs, they present a viable option for large-scale energy storage applications where stringent energy density requirements are less critical [11,12]. The researchers have conducted extensive studies on SIBs, developing various cathode and anode materials as well as electrolyte systems

---

⁎ Corresponding authors at: School of Chemical Engineering and Technology, Xi'an Jiaotong University, Xi'an 710049, China (Wei Tang).
E-mail address: Tang, W. (tangw2018@xjtu.edu.cn)

https://doi.org/10.1016/j.mattod.2025.02.014

Please cite this article in press as: H. Zhang et al., Materials Today, (2025), https://doi.org/10.1016/j.mattod.2025.02.014

[13,14]. Inspired by the commercial success of graphite anodes in LIBs, characterized by low cost and stable performance, graphite has been considered for use in SIB systems. However, sodium ions fail to efficiently insert into the interlayers of graphite to form thermodynamically stable compounds. The lack of suitable anode materials has hindered the commercialization of SIBs [15–17]. Until the year 2000, Dahn addressed this challenge by developing a hard carbon anode through the carbonization of glucose, achieving a high specific capacity of 300 mAh g^{-1}, approaching that of graphite for lithium storage. Despite issues such as low ICE, Dahn's work sparked significant interest in the study of hard carbon anode materials for SIBs [18,19].

Hard carbon materials are commonly regarded as a collective term for carbon materials that are resistant to graphitization [20–22]. Its microstructure consists of short-range disordered microdomains, which are stacks of curved quasi-graphitic microcrystals. These microdomains exhibit random stacking, leaving numerous nanoscale pores. Due to its large interlayer spacing (typically > 0.37 nm) for Na-ion de/intercalation, numerous nanoscale pores for Na-ion ad/desorption [23]. Compared with soft carbon and graphite with long-range order in graphite micro-area, hard carbon with higher defect degree brings more redox active sites, which can store a considerable amount of sodium ions and securely provide higher reversible specific capacity [24,25]. Nevertheless, practical application is hindered by challenges such as the continuous parasitic reactions at the interface between electrode materials and electrolyte, as well as excessive defect sites, lead to the formation of sodium metal clusters by sodium ions, resulting in low initial efficiency [26]. Meanwhile, irreversible adsorption of Na^+ by some active sites will also impair the rate performance and cycling stability [27,28]. Therefore, researchers are dedicated to exploring strategies to address these challenges.

This review provides an overview of principles and strategies developed by researchers in recent years, focusing on regulating the electronic structure and microstructure of hard carbon materials. Fig. 1 summarizes these efforts, primarily categorized into 4 perspectives: (1) Precise control of the amount and types of hybridized atoms to promote surface charge distribution [29,30]. (2) Oxygen functional group regulation as a dynamic strategy to adjust the surface chemical and electrochemical properties of carbon-based materials [31]. (3) Surface coating nanostructure to mitigate side reactions and electrolyte decomposition [32]. (4) Introduction of intrinsic defects to expose more active sites [33]. This review consolidates the current advancements in high-performance hard carbon materials, focusing on hybrid atom doping, oxygen functional group introduction, surface coating, and defect engineering. It covers synthesis strategies, physical characterization, and performance evaluations. Additionally, we discuss the bottleneck issues in the commercialization process of hard carbon anode for SIBs.

Structure and sodium storage mechanisms of hard carbon

Microstructure models of hard carbon

Before delving into the engineering strategies for hard carbon anode materials for SIBs, the review starts with understanding the structures and sodium storage mechanisms of hard carbon. In the realm of carbon materials, amorphous carbon materials are typically categorized into two groups based on their difficulty for graphitization: easily graphitizable carbons and difficult-to-graphitize carbons [11]. Easily graphitizable carbons refer to carbon materials that can be graphitized at temperatures above 2800 , where the disordered structure tends to vanish under high-temperature conditions [24]. Difficult-to-graphitize carbons, also known as hard carbons, exhibit challenges in complete graphitization above 2800 . And its disordered structure is resistant to elimination at high temperatures. Biomass precursors or their derivatives (wood, nut shells, and banana peels, etc.), most carbohydrates (glucose, sucrose, and cellulose, etc.), and synthetic resins readily yield hard carbon during high-temperature carbonization. In contrast, petrochemical raw materials and their downstream products (coal, asphalt, and petroleum coke, etc.) are more likely to form soft carbon under the same conditions [33]. The XRD patterns of four typical carbon materials in Fig. 2(a) reveal that soft carbon, graphite, and reduced graphene oxide exhibit strong (d_{002}) diffraction peaks at 26°, indicating a high degree of graphitization [34]. However, the (d_{002}) peak of hard carbon undergoes a noticeable leftward shift and broadening, suggesting disorder in the stacking of carbon layers. The crystalline stacking differences particularly along the *c*-direction lead to amorphization. Fig. 2(b) reflects the difference of amorphous carbon and graphitic carbon. Notably, the presence of tiny and curved graphene sheets in hard carbon structure can typically form short-range ordered microdomains that parallelly stack. The stacking layers are normally limited to 2–6 layers, with a lateral size constraint of 4 nm [35,36]. These microdomains exhibit long-range disorder, forming abundant nanoscale pores between microdomains of different orientations [37]. The interlayer spacing of hard carbon's (d_{002}) plane is typically between 0.37 and 0.40 nm, significantly larger than graphite's 0.33 nm [38,39].

As widely recognized, hard carbon lacks standardized structural features, making it complex to establish a universal hard carbon structure model. Over the past decades, several representative hard carbon structure models have been proposed, as depicted in Fig. 2(c). Franklin et al. [41] described hard carbon as randomly oriented graphite nanodomains surrounded by non-graphitizable carbon in 1951. These non-graphitizable regions, acting as linking points, inhibit further graphitization of the material and lead to the generation of numerous micropores. While this model is significant for understanding the properties of two-dimensional hard carbon structures, it still struggles to explain the intricate three-dimensional microstructure. In 1975, Ban et al. [42] proposed a model consisting of interleaved, curved graphite nanoribbons. However, it fails to explain non-graphitizable features of hard carbon. With the advancement of computational capabilities, this model has gradually been refined. Townsend et al. [43] suggested the presence of fullerene-like structures in hard carbon, which was later confirmed by Harris in 1997 through high-resolution transmission electron microscopy (HRTEM). Terzyk et al. [44,45] discussed a new hard carbon model composed of discrete curved carbon layers in 2007. The model highlights that in the curved carbon structure, the random dispersion of pentagonal and heptagonal

Please cite this article in press as: H. Zhang et al., Materials Today, (2025), https://doi.org/10.1016/j.mattod.2025.02.014

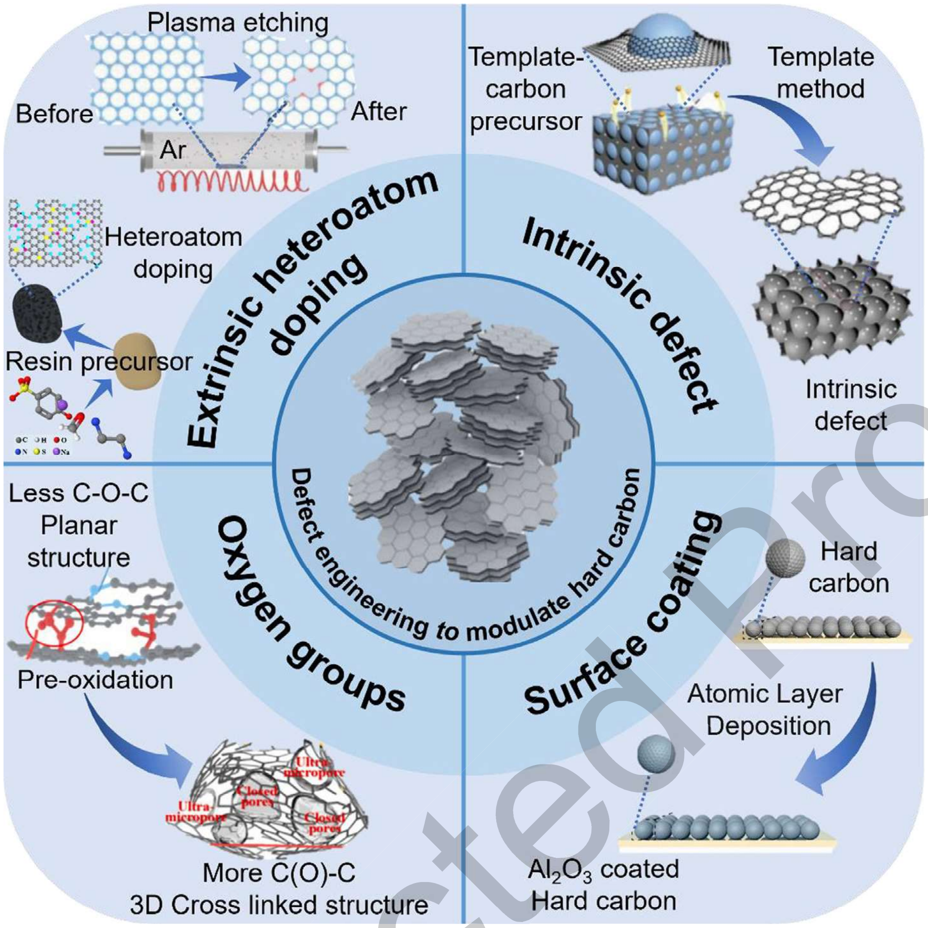

FIG. 1

A summary of defect engineering strategies for hard carbon materials.

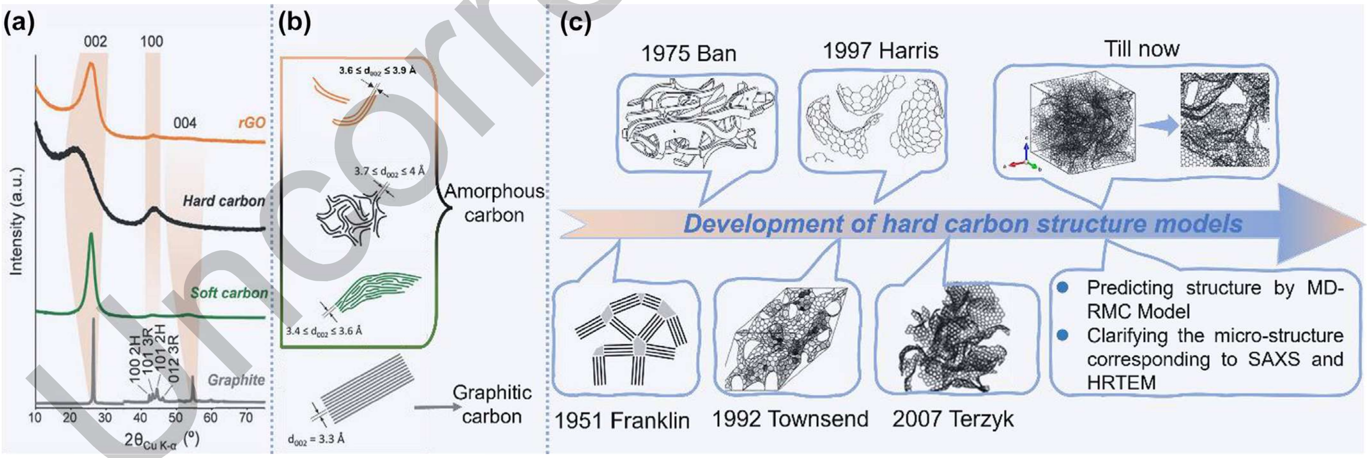

FIG. 2

The type of classical carbon materials. (a) XRD patterns of rGO, hard carbon, soft carbon and graphite. (b) The interlayer spacing of different carbon materials. (c) The development of several representative hard carbon structure models. Reproduced with permission [24,40]. Copyright 2018 and 2022, Wiley-VCH.

structures stabilizes the curvature, preventing the graphitization of hard carbon. Up to now, Surta et al. [40] has generated structural models by combining molecular dynamics and reverse Monte Carlo methods to fit pair distribution functions (PDFs). From this model, it is possible to identify and quantify the types and quantities of structural features of hard carbon and associate them with Galvanostatic charge/discharge (GCD) curves to explore sodium storage mechanisms. This achieves the level of fingerprint recognition for hard carbon structures.

Despite the progress made in hard carbon structure models, none has been widely accepted until the year 2000 when Dahn et al. [46] introduced the "house of cards" structural model for

Please cite this article in press as: H. Zhang et al., Materials Today, (2025), https://doi.org/10.1016/j.mattod.2025.02.014

the first time. In this model, the microscopic structure is formed by the random stacking of numerous disordered microcrystalline carbon layers, accompanied by a significant number of nanoscale pores. This "house of cards" model marked breakthrough in understanding Na-ion storage mechanism in hard carbon anode for SIBs.

Sodium storage mechanism of hard carbon anode

To achieve the functional design of a high-performance hard carbon (HC) anode, it is crucial to gain a deep understanding of the relationship between the microstructure and sodium storage performance. Various interpretations exist for the high-voltage sloping region and low-voltage plateau observed in the GCD curves of hard carbon [47–49]. Currently, the proposed sodium storage mechanisms can be summarized into the following four pathways:

Fig. 3(a) depicts the "Adsorption-Filling" mechanism. Xu et al. [50] proceeding from the structure and electrolyte aspects, investigated the sodium storage behavior and performance of hard carbon by employing sulfur filling, manipulating pyrolysis temperature and electrolyte systems. The results revealed that the sulfur filled into the micro-pores of hard carbon without affecting the structure of graphitic microcrystalline layers of hard carbon. However, the low-voltage plateau below 0.1 V (vs Na^+/Na) disappeared, exhibiting discharge/charge plateaus at 1.3/1.6 V (vs Na^+/Na), illustrating that the capacity in the plateau region originates from the filling of Na^+ into the micro-pores. By altering the carbonization temperature, they prepared HC-1000 with a high concentration of defects/heteroatoms and a highly amorphous structure, and HC-2000 with enhanced graphitic structure and reduced defects/impurities. The reduction in defects and heteroatoms of hard carbon corresponded to a decreasing capacity in the sloping region, indicating that the adsorption of Na^+ on defect sites and heteroatoms contributes to the capacity of sloping region.

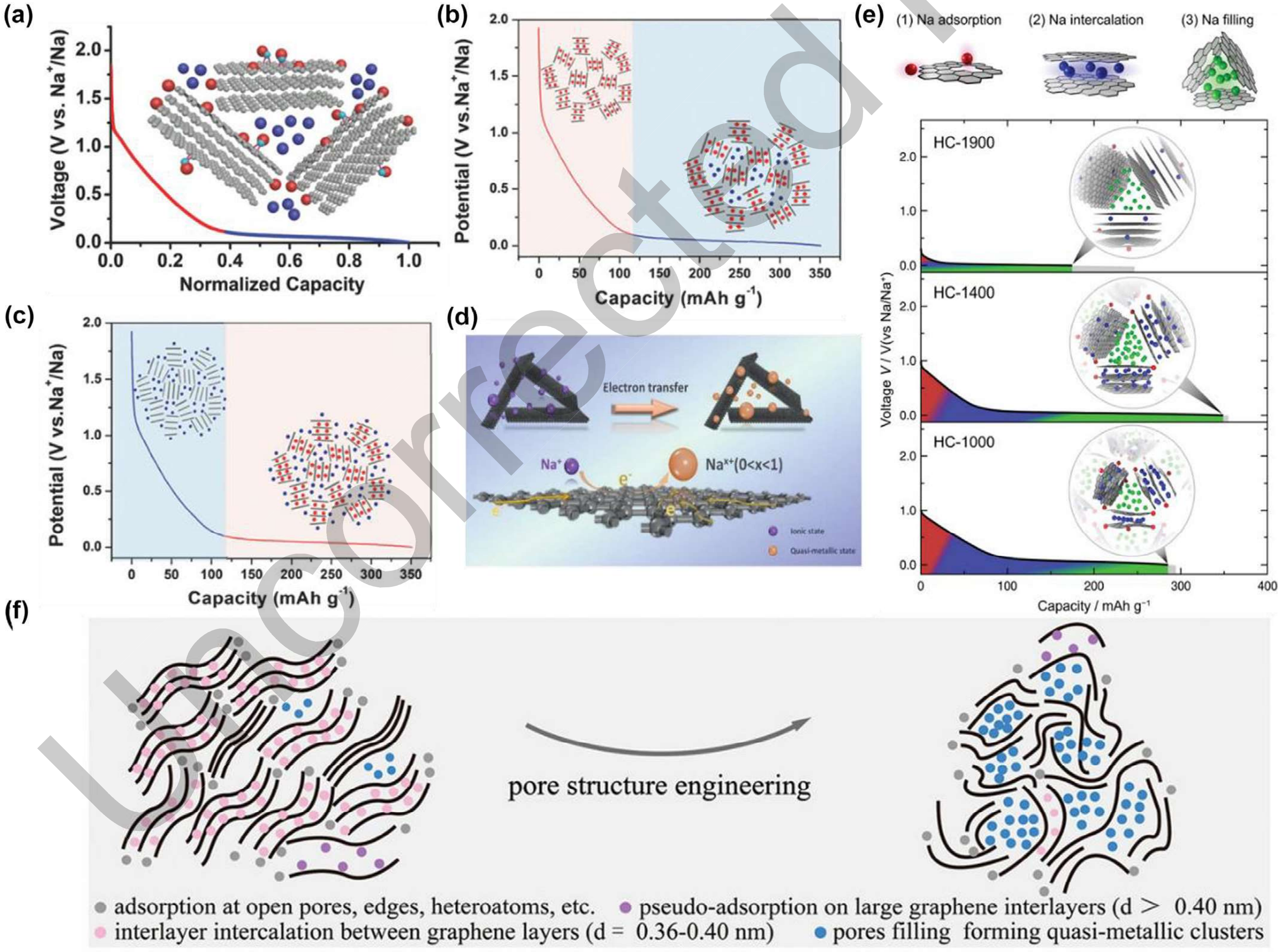

FIG. 3

Schematic illustration of Sodium Storage Mechanism in Hard Carbons (a) The "Adsorption-Filling" mechanism. Reproduced with permission [50]. Copyright 2018, Wiley-VCH. (b) The "Insertion-Filling" mechanism. (c) The "Adsorption-Insertion" Mechanism. Reproduced with permission [54]. Copyright 2017, Wiley-VCH. (d) The diagram of sodium in hard carbon with "quasi-metallic" state. Reproduced with permission [56]. Copyright 2021, Wiley-VCH. (e) The "Adsorption-Insertion-Filling" mechanism. Reproduced with permission [53]. Copyright 2019, Wiley-VCH. (f) The influence of microstructure on sodium storage mechanism. Reproduced with permission [59]. Copyright 2022, Wiley-VCH.

Please cite this article in press as: H. Zhang et al., Materials Today, (2025), https://doi.org/10.1016/j.mattod.2025.02.014

The "Insertion-Filling" mechanism is illustrated in Fig. 3(b). Dahn et al. [46] proposed that the high-voltage (0.1–1.2 V, vs Na^+/Na) sloping region corresponds to the insertion of Na^+ between the carbon layers, similar to the GCD curve of expanded graphite [51]. The insertion voltage reduces with increasing insertion amount. The low-voltage (0–0.1 V, vs Na^+/Na) plateau region capacity is related to the filling behavior of Na^+ in the nanoscale graphitic microcrystalline regions with disordered stacking micro-pores. Komaba utilized Ex-situ X-ray diffraction (XRD) to investigate the relationship between the interlayer spacing of hard carbon materials and the redox potential [52]. When the Na^+ intercalation potential dropped to 0.2 V (vs Na^+/Na), the hard carbon (d_{002}) diffraction peak shifted from 23.4° to 21°, indicating an increase in carbon interlayer spacing due to Na^+ intercalation. Upon charging to 2 V, the peak position restored, indicating reversible insertion and extraction of Na^+ between the graphitic layers [53]. Additionally, when discharging voltage was below 0.2 V, SAXS (small-angle X-ray scattering) analysis revealed a decrease in electron density in the range of 0.03–0.07 Å, suggesting that the low-potential plateau corresponds to the filling of Na^+ in the micro-pores.

Fig. 3(c) describes the "Adsorption-Insertion" mechanism. Cao et al. [54,55] by pyrolyzing polyaniline to obtain tubular hard carbon, observed a decreasing trend in sodium storage capacity in the sloping region as the pyrolysis temperature increased, correlating with a reduction in carbon layer defects. They concluded that the high-potential sloping region corresponds to the adsorption of Na^+ hard carbon defect sites. Through in-situ XRD testing, they observed changes in carbon layer spacing in the low-voltage plateau region, inferring the formation of Na-C compounds due to the insertion of Na^+ between the graphite layers. Theoretical calculations indicated that the interlayer spacing after Na^+ insertion was between 0.37–0.47 nm.

Based on previous research, the "Adsorption-Insertion-Filling" mechanism was verified, as represented in Fig. 3(d and e). Wu et al. [56] observed an electrode color change and the generation of bubbles when electrode films at various sodium-storing states reacted with an ethanol solution containing phenolphthalein. Gas chromatography confirmed the presence of hydrogen gas. As the discharge depth of the electrode film increased, the concentration of Na^+ and its ion conductivity gradually raised. Conversely, with the increasing charge of the electrode film, the concentration of Na^+ and ion conductivity decreased. Based on these experimental results, they proposed a mechanism that Na^+ are stabilized and stored in the interior of hard carbon materials in a "quasi-metallic" form shown in Fig. 3d [48,57]. Through SAXS and WAXS (wide-angle X-ray scattering) analysis (Fig. 3e), Yamada [53] found that hard carbon prepared at a lower temperature of 1000 retained a significant number of defects, resulting in a larger capacity in the sloping region due to Na^+ adsorption at defect sites. At 1400 , the Na^+ insertion capacity in the graphite domains of hard carbon was larger because the interlayer spacing in graphitic microcrystalline layers exceeded the threshold for sodium insertion (>3.6 Å). At a higher temperature of 1900 , the capacity derived from nanoscale pores increased, but the actual capacity was limited by the slow kinetics. Therefore, to avoid excessive graphitization, the "Adsorption-Interlayer-Filling" sodium storage mechanism can effectively corroborate these experimental results [58].

After comprehensive analysis, Cao and co-workers[59] summarized that the sodium storage mechanism in the sloping segment, as shown in Fig. 3(f), is generally attributed to the adsorption process of Na^+. The adsorption sites include open pores, edges positions near heteroatoms, and larger interlayer spacings (>0.4 nm). The sodium storage mechanism in the plateau region involves intercalation storage of Na^+ in graphitic layers (0.36 ~ 0.40 nm) and the deposition of Na^+ to form cluster-like metallic sodium in closed pores [60].

Modulation of hard carbon anode by defect engineering

Given the physicochemical characteristics of hard carbon (HC) and its inherent shortcomings, numerous material engineering strategies have been reported. The effectiveness of these modifications has been validated. The optimization strategies for hard carbon defect engineering can be summarized as external heteroatom doping [61], introduction of oxygen functional groups [62], surface coating [63], and intrinsic defect management [37].

Extrinsic heteroatom doping

The limited active sites of hard carbon restrict the adsorption of Na^+, preventing it from achieving satisfactory capacity and rate performance in practical applications [64]. As shown in Fig. 4, introducing heteroatoms (N, S, P, B) and metal atoms (Zn single atom, etc.) via different treatment methods can optimize the interlayer spacing, surface wettability, electron conductivity, and other microscopic properties of hard carbon materials. Furthermore, increasing the spacing of graphitic interlayer facilitates the insertion of larger-radius Na^+. Introducing heteroatoms and defects into the carbon lattice induces capacitive adsorption for rapid sodium storage. Optimizing the pore network ameliorates the transport and storage of Na^+, thereby improving its sodium storage performance [65–69].

Currently, general doping methods in research include the direct carbonization of compounds rich in heteroatoms, as illustrated in Fig. 4(a-b). Zhou et al. [70] successfully prepared nitrogen-doped hard carbon microspheres in a one-step process using an aniline-formaldehyde condensation reaction with aniline and formaldehyde as precursors. Electrochemical tests also reflected that nitrogen doping introduced more defects for Na^+ adsorption. Ma et al. [71] utilized polyacrylonitrile, a nitrogen-containing polymer, as a precursor and employed electrospinning and low-temperature carbonization to produce nitrogen-doped hard carbon nanofibers. This direct in-situ doping strategy in the carbon matrix enhances target material productivity. In addition to in-situ doping strategies, post-treatment doping is another imperative approach for introducing heteroatoms. In Fig. 4(c), Jiang and co-workers[72] constructed an oxygen-free reaction system. They used hexane as a carbon source for high-temperature pyrolysis to prepare carbon materials via chemical vapor deposition. Subsequently, phosphorus doping with an ultra-high weight ratio was achieved by using phosphorus trichloride as the phosphorus source. The carbon material demonstrated excellent rate performance in electrochemical

Please cite this article in press as: H. Zhang et al., Materials Today, (2025), https://doi.org/10.1016/j.mattod.2025.02.014

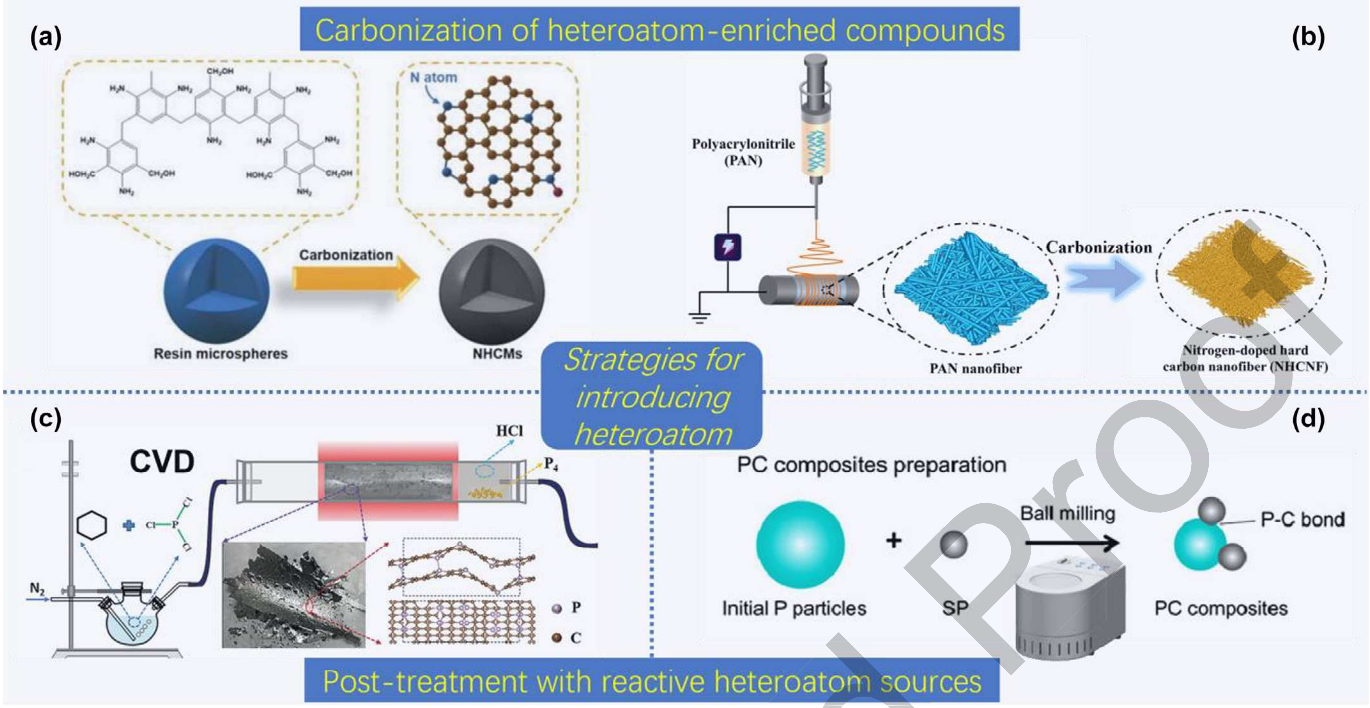

FIG. 4

Strategy of introducing heteroatoms into hard carbon materials. (a) Carbonized nitrogen-containing resin microspheres. Reproduced with permission [70]. Copyright 2023, Wiley-VCH. (b) Carbonized PAN nanofibers prepared by electrospinning. Reproduced with permission [71]. Copyright 2023, Wiley-VCH. (c) Using chemical vapor deposition to deposit phosphorus on pyrolytic carbon materials. Reproduced with permission [72]. Copyright 2021, Wiley-VCH. (d) Utilizing ball milling to achieve P-C composite. Reproduced with permission [73]. Copyright 2021, Elsevier.

tests. Furthermore, Rummeli et al. [73] produced P-C composite materials through ball milling with different durations of red phosphorus and Super P (Fig. 4d), leveraging weak interactions such as van der Waals forces. The sodium storage mechanism was enhanced by red phosphorus alloying, contributed to an ultra-high specific capacity (2593 mAh g^{-1}), ultimately achieving a full-cell energy density of 134 Wh kg^{-1}.

Research on heteroatom doping has evolved from an initial focus on doping performance to a deeper understanding of underlying mechanisms, whether through in-situ doping via the carbonization of heteroatom-rich compounds or post-treatment doping methods like chemical vapor deposition (CVD) and ball milling. We will now delve into a detailed discussion regarding the various forms of heteroatom doping and their impact on performance.

The extensive research on heteroatom-doped carbon as anode materials for sodium-ion batteries is primarily driven by the goal of expanding interlayer spacing and enhancing electrical conductivity [74–77]. Nitrogen is one of the most extensively studied heteroatom elements. In order to gain further insight into the impact of nitrogen-doped hard carbon on the performance of sodium-ion batteries, Lu et al. [65] synthesized a precursor through the polymerization reaction of trisodium citrate and hexamethylenetetramine. This precursor was then subjected to pyrolysis to produce nitrogen-induced highly stable and abundant pyridinic N-doped three-dimensional hard carbon, as shown in Fig. 5(a), utilized as the anode for sodium-ion batteries. To comprehensively understand the effect of nitrogen introduction into the carbon matrix on sodium storage, combined with density functional theory (DFT) calculations, Fig. 5(b) revealed that different nitrogen-doping sites, N-6, N-Q, and N-5, all exhibited lower diffusion barriers than pristine hard carbon. This implied that the introduction of free radicals improves the kinetics of sodium ion adsorption. The rate performance, as depicted in Fig. 5(c), also showed a significant enhancement, providing a discharge capacity of 238 mAh g^{-1} at a current density of 5A g^{-1}. Furthermore, the electron paramagnetic resonance (EPR) spectra, illustrated in Fig. 5(d), exhibited subtle changes at high potentials (1.2–0.1 V). However, a sharp decrease in intensity was observed between 0.1 V and 0.01 V, indicating the insertion of Na^+ into the interlayers of graphitic microcrystals. As the charging process progressed, the intensity recovered to its original state, suggesting that the free radicals introduced by nitrogen doping contribute to a highly reversible adsorption of Na^+ [78–80].

Compared to nitrogen, sulfur atoms have a larger radius and exhibit electrochemical activity, enabling reversible reactions with sodium to provide higher capacity [81,82]. Jiang et al. [66] synthesized hard carbon material with an exceptionally high sulfur content of 62.28 wt% using a one-step pyrolysis method by mixing 1,4,5,8-naphthalenetetracarboxylic dianhydride (NTCDA) with sulfur powder, which was designated the sulfur-doped disordered carbon (DC-S) as depicted in Fig. 5(e). For comparison, the disordered carbon (designated as DC-S) was prepared by the same method without sulfur powder. XRD analysis revealed that sulfur-doped carbon increases the interlayer spacing, and X-ray Photoelectron Spectroscopy (XPS) results confirmed the formation of thiophene-sulfur bonds, providing

Please cite this article in press as: H. Zhang et al., Materials Today, (2025), https://doi.org/10.1016/j.mattod.2025.02.014

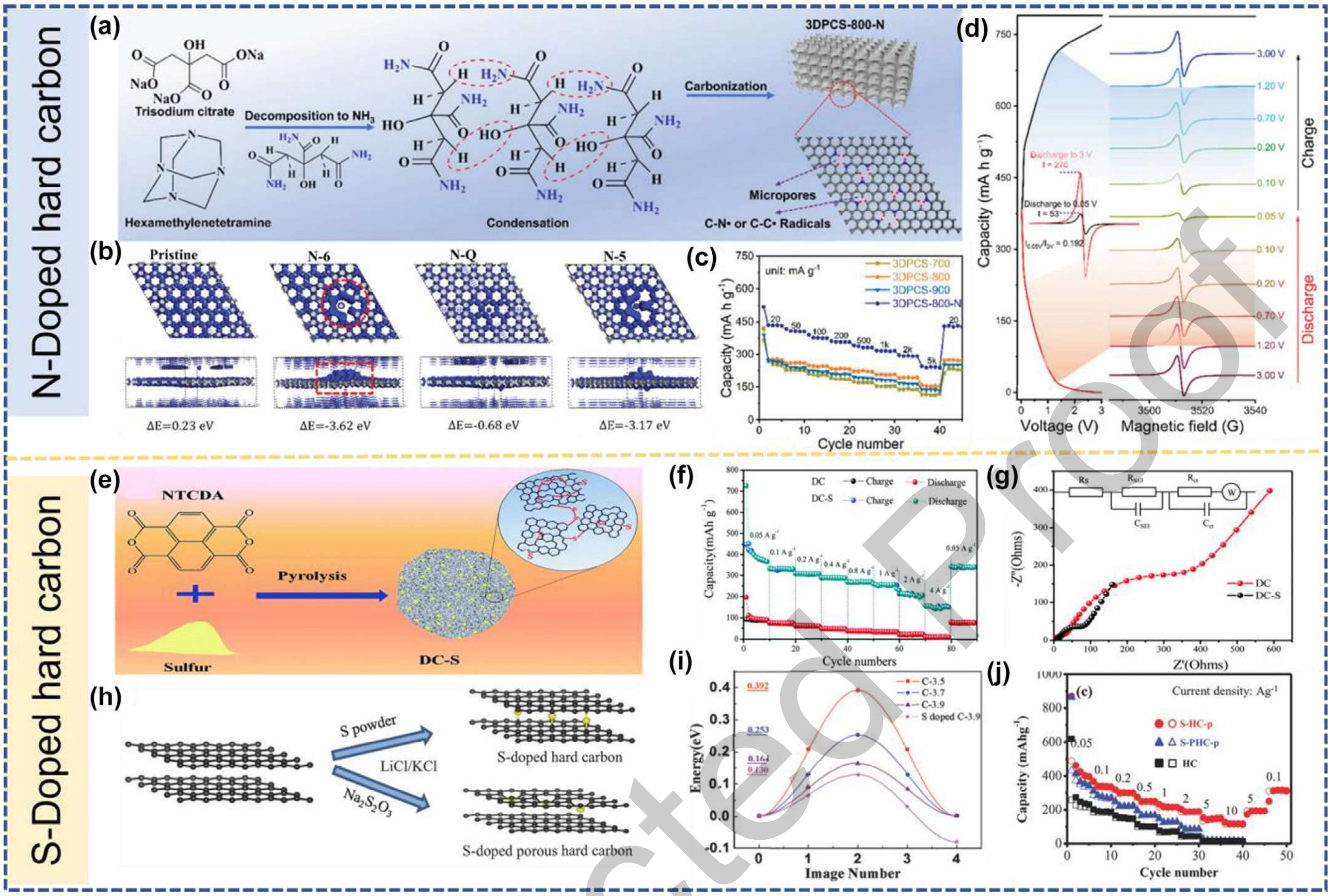

FIG. 5

(a) The schematic for preparation process of N-doped hard carbon. (b) The different electron density of various calculated models. (c) Rate performance of hard carbon anodes. (d)The ex-situ EPR spectra of different charge–discharge voltage platforms. Reproduced with permission [65]. Copyright 2021, Wiley-VCH. (e) The illustration for preparation procedure of S-doped hard carbon. (f) The rate capability of DC and DC-S. (g) Nyquist plots of DC and DC-S. Reproduced with permission [66]. Copyright 2015, Royal Society of Chemistry. (h) The fabrication of different S-doped sites hard carbon. (i) The different interlayer distances and S doping barrier energy. (j) The rate capability of pristine HC and different S-doped sites hard carbon. Reproduced with permission [82,83]. Copyright 2018, Wiley-VCH.

pathways for rapid electron transfer. Fig. 5(f) demonstrates a reversible capacity of 211mAh g^{-1} at a current density of 4 A g^{-1}, and impedance tests showed smaller charge transfer resistance in Fig. 5(g), attributed to the adjustment of the electronic structure of adjacent C atoms and enhanced electron conductivity in the sulfur-doped carbon matrix. Regarding the influence of different sulfur-doping sites, Zhang et al. [83] utilized sulfur powder and sodium thiosulfate as distinct sulfur sources to achieve interlayer doping and intralayer doping, as shown in Fig. 5(h). Regarding the influence of different sulfur-doping sites, theoretical calculations confirmed that interlayer sulfur doping achieves a lower Na^+ diffusion barrier of 0.13 eV, along with a wider interlayer spacing of 0.3997 nm (compared to 0.3695 nm for intralayer doping), consequently contributed to superior rate performance in Fig. 5(i). At an extremely high current density of 10 A g^{-1}, the reversible capacity reached 175 mAh g^{-1}. This study also affirmed that, in terms of sulfur doping sites, interlayer doping exhibits superior electrochemical performance compared to intralayer doping in Fig. 5(j).

While sulfur doping could contribute to additional sodium storage capacity, its higher redox potential in reaction with sodium is unfavorable for preparing high-energy–density full cells [81]. Phosphorus, on the other hand, is chosen as a doping element for modifying hard carbon anodes due to its ability to provide an ultra-high theoretical sodium storage capacity (2596mAh g^{-1}) [73,84–86]. Wu and co-workers[87] utilized polyvinylpyrrolidone (PVP) as a carbon source and H_3PO_4 as a phosphorus source to synthesize a precursor via electrospinning method, followed by high-temperature carbonization to prepare phosphorus-doped hard carbon, as depicted in Fig. 6(a). DFT calculations indicated that the strengthening of P=O and P—C bonds enhanced the binding energy of hard carbon with Na^+, improving the adsorption capacity at low voltage platforms. The significantly higher density of states (DOS) for O atoms compared to P atoms, as shown in Fig. 6(b-c), also suggested that the introduction of phosphorus improved Na^+ adsorption capacity [88]. Rate performance also reflected a significant increase with phosphorus doping. Especially at a high current density of 2 A

Please cite this article in press as: H. Zhang et al., Materials Today, (2025), https://doi.org/10.1016/j.mattod.2025.02.014

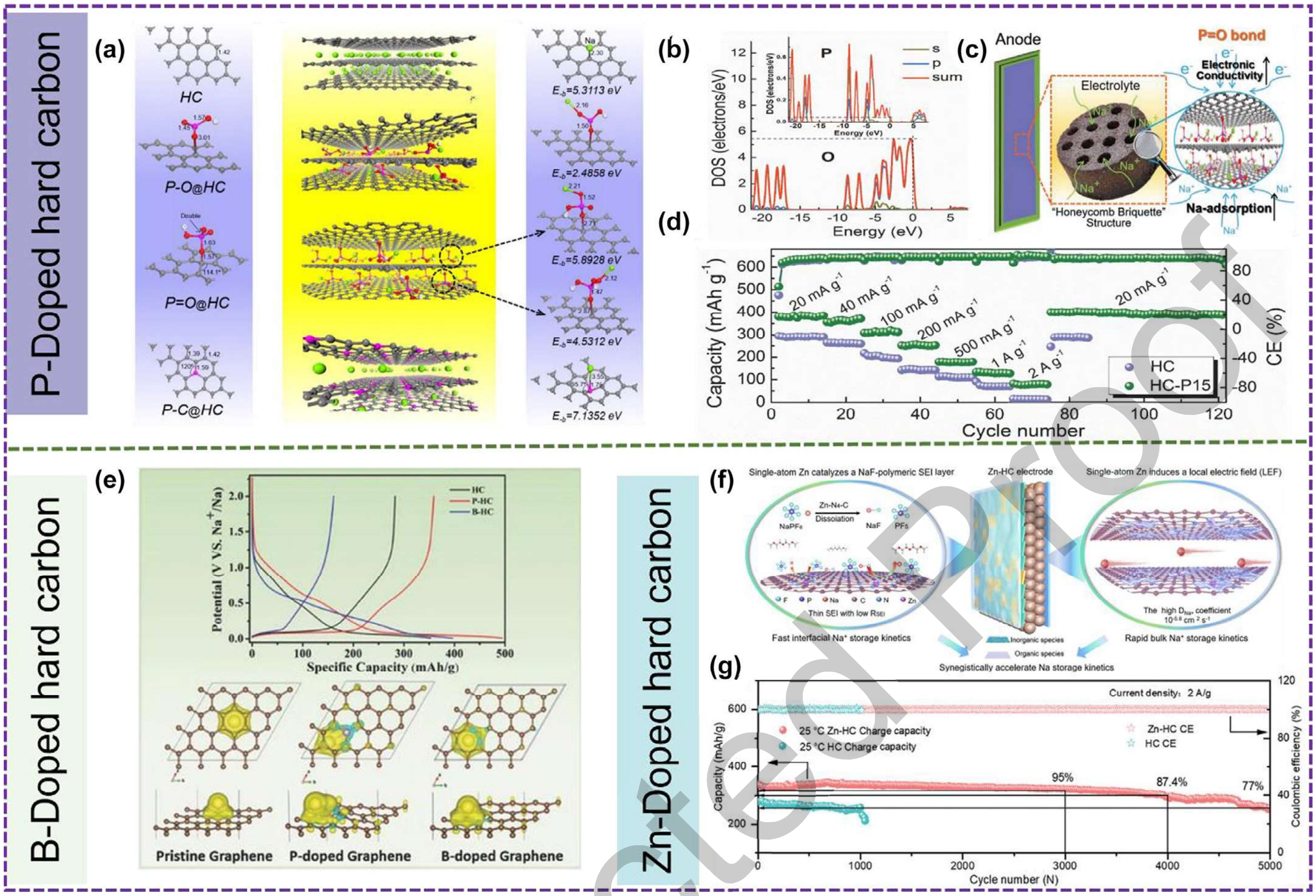

FIG. 6

(a) Before and after phosphorous-functionalized hard carbon structure, and Na^+ adsorption energies of different structure models. (b) The comparison of DOS of P atom and O atom. (c) The illustration of phosphorus-functionalized hard carbon anode with superior electrochemical performance. (d) The rate performance of pristine HC and P-doped HC. Reproduced with permission [87]. Copyright 2018, Wiley-VCH. (e) The first discharge–charge profiles of P-doped, B-doped carbon materials. And charge distribution models of different carbon materials. Reproduced with permission [89]. Copyright 2017, Wiley-VCH. (f) The illustration of synergistically accelerate Na^+ transmission dynamics. (g) The cycling stability of HC and Zn-HC. Reproduced with permission [69]. Copyright 2021, Wiley-VCH.

g^{-1}, it could still exhibit a specific capacity of 120 mAh g^{-1}, as shown in Fig. 6(d).

Boron-doped hard carbon materials are typical p-type doped materials due to hole doping effects, resulting in more electronic states and a lower Fermi level, which is adverse to cation transport [68]. Ji et al. [89] used a mixture of boric acid and sucrose as a precursor to obtain boron-doped hard carbon through dehydration and thermal decomposition. Neutron total scattering combined with DFT calculations revealed that boron doping is an in-plane doping, and the boron-doped atoms themselves acted as strong "defects" binding sodium ions. Fig. 6(e) depicted that boron-doped hard carbon has a longer sloping discharge platform. However, the strong binding energy affected the release of sodium ions during the first charge, leading to a reduced initial Coulombic efficiency (ICE = 23 %). Higher cut-off voltage was required to completely remove sodium ions, reflecting that boron doping was not a prevalent method for utilizing hard carbon defect engineering modification [90].

In addition to nonmetallic elements, recent investigation has also focused on metallic elements for single-element doping. Taking advantage of lower metal coordination numbers and easily tunable electronic structures, Zhao et al. [69] constructed hard carbon materials doped with single-atom zinc. The optimized hard carbon material in Fig. 6(f) presented an expanded graphite area, DFT calculation revealed the Zn-N_4-C configuration decreases the dissociation energy (Ed) for P─F bond breaking (1.62 eV) on the Zn-HC surface compared to the vacancy defects (HC, 2.55 eV). This demonstrates that the Zn-N_4-C configuration facilitates the decomposition of $NaPF_6$, enhancing the reaction of Na^+ with electron-rich fluorine to form NaF compounds within the solid electrolyte interface (SEI) layer during charge–discharge cycles. Furthermore, the local electric field triggered by single-atom zinc also accelerates sodium ion transport. Even after 3000 cycles, the material retained 95 % of its initial capacity, as shown in Fig. 6(g), demonstrating excellent long-term cycling performance. The assembled full cell achieved an ultra-high energy density of 323 Wh kg^{-1}.

Besides single-atom doping strategies, the co-doping of different functional dual or multiple heteroatoms represents a novel approach to achieving high electrochemical performance in hard

Please cite this article in press as: H. Zhang et al., Materials Today, (2025), https://doi.org/10.1016/j.mattod.2025.02.014

carbon anodes. The synergistic effects of dual or multiple heteroatom co-doping can facilitate the intrinsic transfer characteristics of sodium ions and electrons within the graphite microcrystal structure, thereby accelerating reaction kinetics and achieving ideal Na^+ storage performance [91–95].

Zhang and co-workers[96] prepared N/S co-doped carbon microspheres (NSC-SP) through the pyrolysis of cellulose and aniline polymerized with dodecyl benzene sulfonic acid (DBSA), as depicted in Fig. 7(a). Fig. 7(b-c) exhibited that compared to the undoped sample, the N/S co-doped sample presented higher reversible capacity and better rate performance. The charge capacity of the 3200 cycles long-term cycling at a current density of 0.5 A g^{-1} almost remained constant at 150mAh g^{-1} with negligible decay. Theoretical calculations in Fig. 7(d) demonstrated that N/S co-doping generated more in-plane defects and extended the interlayer spacing of carbon. The density of states (DOS) near the Fermi level increased with N/S co-doping, resulting in higher electron conductivity.

To achieve rapid charge and discharge along with higher energy density, Huang et al. [97] designed a nitrogen and phosphorus co-doped three-dimensional cross-linked hard carbon network, as illustrated in Fig. 7(e). Nitrogen was introduced to adjust the electronic structure and defect sites, while the larger radius of phosphorus led to a highly distorted carbon structure, expanding the interlayer spacing and enhancing sodium ion insertion and pore filling [98–100]. The synergistic effects of both nitrogen and phosphorus doping comprehensively improved the sodium storage performance, as shown in Fig. 7(f). Theoretical calculations in Fig. 7(g) vividly depicted that the introduction of phosphorus atoms enhanced the system's electron donor ability, with more charge accumulation, strengthening the adsorption of sodium ions. The density of states further revealed that N/P co-doped hard carbon possessed the higher Fermi level, contributing to an enhancement in electrochemical performance [101,102]. Recent Sun et al. [103] further corroborated that the incorporation of additional P doping leads to an augmentation in the pyridinic-N content. DFT calculations unveiled that pyridinic-N possesses the highest Na^+ adsorption potential when compared to pyrrolic-N and graphitic-N, thereby facilitating a more efficient Na^+ adsorption process. Furthermore, P doping widened the interlayer spacing of the carbon matrix, reducing Na^+ diffusion resistance. Electrochemical tests ultimately demonstrated that the designed N/P co-doped hard carbon spheres exhibit fast and efficient sodium storage.

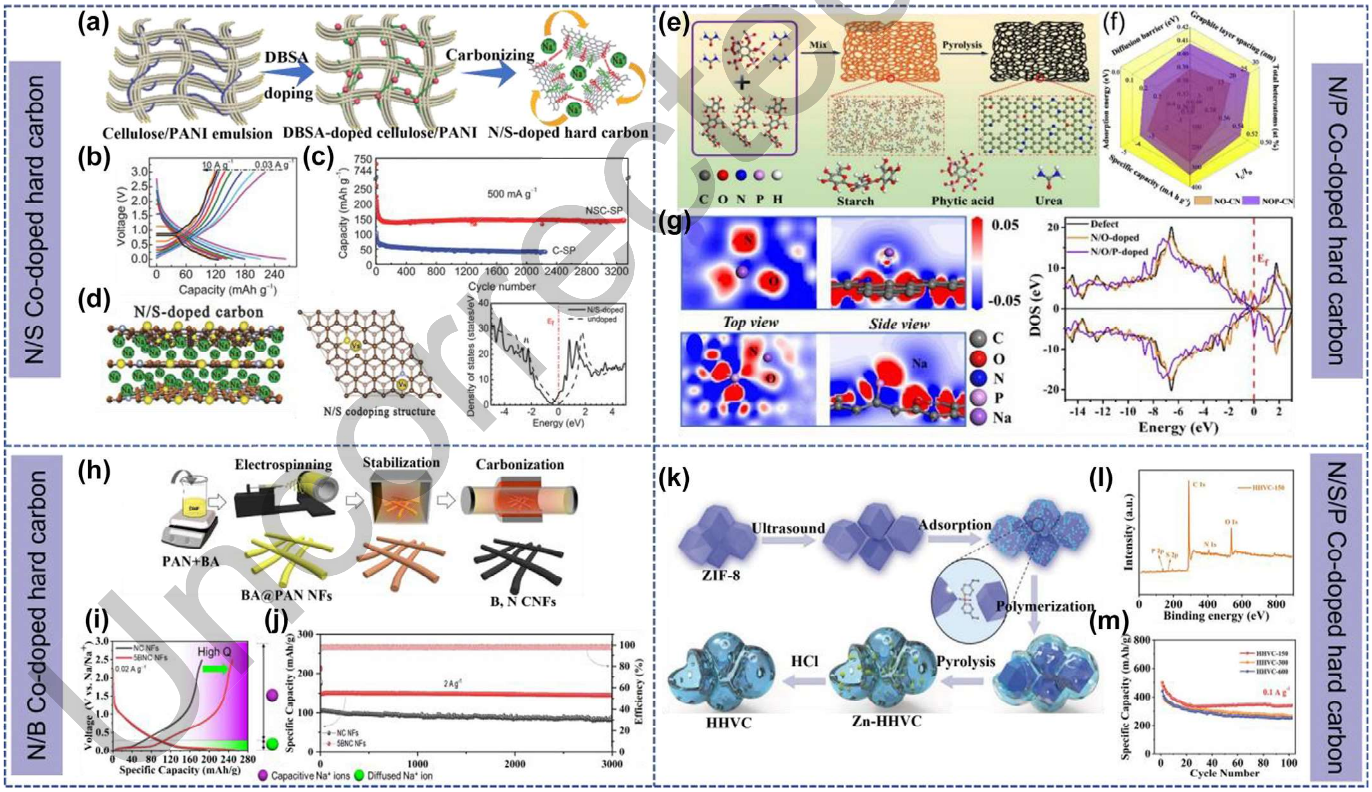

FIG. 7

(a) The illustration of fabrication procedure for N/S-doped hard carbon. (b) Charge–discharge curves of N/S-C at various current densities. (c) The comparison of cycling performance at 500 mA g^{-1}. (d) Effect of N/S co-doped hard carbon on layer structure change and density of states of the undoped and N/S co-doped hard carbon. Reproduced with permission [96]. Copyright 2016, Wiley-VCH. (e) The schematic illustration of synthesis for N/P co-doped carbon network. (f) The comparison of physical and electrochemical properties of N doped carbon and N/P co-doped carbon. (g) The sodium ions adsorption energy and density of states for various doped carbon materials. Reproduced with permission [97]. Copyright 2020, Elsevier. (h) The Schematic of preparation process for N/B co-doped carbon nanofibers. (i) The first charge–discharge curve of N doped and N/B co-doped carbon nanofibers. (j) The cycling performance at current density of 2 A g^{-1}. Reproduced with permission [104]. Copyright 2023, Elsevier. (k) The schematic of the synthesis of N/S/P tri-doped hierarchical vesicular carbon. (l) XPS survey of N/S/P tri-doped hierarchical vesicular carbon. (m) The cycling capability at 0.1 A g^{-1} of various anode materials. Reproduced with permission [105]. Copyright 2018, Wiley-VCH.

Please cite this article in press as: H. Zhang et al., Materials Today, (2025), https://doi.org/10.1016/j.mattod.2025.02.014

Some research progress has also been made in the field of nitrogen and boron co-doping. Cho et al. [104] utilized nitrogen-doped carbon framework to form pyridinic nitrogen and pyrrolic nitrogen, improving the wettability and sodium storage active sites of hard carbon fibers. Simultaneously, boron was employed to lower the material's Fermi level and the lowest unoccupied molecular orbital, enabling the hard carbon to accept and absorb more electrons from sodium. Using boric acid and polyacrylonitrile as the precursors for electrospinning, solidification, and carbonization, boron-nitrogen in-situ doped hard carbon nanofibers (BNC NF) XPS were obtained, as shown in Fig. 7(h). BNC NF exhibited excellent sodium storage capacity, with a reversible capacity increase of 80 mAh g^{-1} at a current density of 20 mA g^{-1} in the high voltage range. Which attributed to the lowering of the Fermi level due to boron doping, as depicted in Fig. 7(i). Additionally, at a high current density of 2A g^{-1}, long-term cycling stability improved, attributed to nitrogen doping optimizing defects and increasing reversible adsorption, as shown in Fig. 7(j).

The performance of dual-heteroatom-doped hard carbon materials has been confirmed to be superior to that of singly-doped hard carbon materials [106,107]. Similarly, researchers have made corresponding progress in the development of triple-heteroatom-doped electrode materials. Ji et al. [105] utilized hexachloro-cyclotriphosphazene (HCCP) and 4,4′-sulfonyldiphenol (BPS) polymerized on the surface of ZIF-8 as carbon precursors. After carbonization and acid washing to remove ZIF-8, they prepared N/S/P tri-doped hierarchical vesicular hard carbon material, as shown in Fig. 7(k). XPS characterization revealed nitrogen, sulfur, and phosphorus contents of 3.38 %, 0.94 %, and 2.12 %, respectively. Fine spectra also confirmed the in-situ doping of nitrogen, sulfur, and phosphorus into the carbon lattice, as depicted in Fig. 7(l). By adjusting the amount of precursors HCCP and BPS, the wall thickness of the vesicles was controlled. Fig. 7(m) showed that the electrochemical tests demonstrated that HHVC-150 with an 18 nm wall thickness exhibited the optimal reversible capacity of 327 mAh g^{-1} at a current density of 0.1 A g^{-1}.

From our perspective, although the doping methods vary, the enhancement of the electrochemical performance of heteroatom-doped hard carbon materials can be attributed to four main factors: 1) increased defects, distortions, and enlarged interlayer spacing caused by different atomic radius; 2) adjustments in electron distribution leading to enhanced Na^+ adsorption and electron conductivity; 3) the generation of additional active centers and reaction sites by heteroatoms; 4) the synergistic effects among heteroatoms [108–110]. The study of doping to improve sodium storage in hard carbon can comprehensively consider the aforementioned factors. Heteroatom doping strategies are widely used in laboratory research, enabling better rate performance, long-cycle stability under high current, and higher energy density. However, compared to pristine hard carbon, which can achieve an initial coulombic efficiency (ICE) ≥ 90 % [111,112], doping is often achieved at the expense of a reduction in ICE [113,114], complicates the manufacturing process, and reduces the cost advantage of sodium-ion batteries [115]. Therefore, the development of simple and easy-to-operate doping modification methods is highly anticipated for future commercialization. Furthermore, we summarize diverse categories of heteroatom-doped hard carbon anodes and its specific functions, effects and properties for SIBs in Table 1, in order to batter comprehend the influence of different doping.

Oxygen functional groups

The introduction of heteroatoms such as N, S, P, and B into the carbon framework could increase the interlayer spacing, preserving sufficient space for the insertion and filling of sodium ions [95]. Simultaneously, the implantation of electronegative atoms can enhance electrochemical activity [62]. Grafting surface functional groups may facilitate both the diffusion-controlled bulk process and the surface-limited capacitive process [23]. Further refinement reveals that the surface-controlled capacitance process corresponds to the sloping charge–discharge segment in the high-voltage region, while the diffusion-controlled bulk process directly influences the charge–discharge process in the low-voltage plateau region [116,117]. Achieving a balanced adjustment of the two processes through the rational implantation of functional groups realizes the optimal design of electrode materials. The introduction of oxygen functional groups on the surface of hard carbon, in particular, has garnered widespread attention. Oxygen-containing groups are the most common functional groups in materials, introduced either from carbon precursors or oxidizing environments, and can coexist with other doping elements [118]. Recent research has conducted numerous experimental and computational studies to elucidate the role of oxygen-containing functional groups in the Na^+ storage process in hard carbon.

Depending on the characteristics of the precursor, oxygen functional groups are introduced in diverse manners. Chen et al. [119] utilized asphalt as the precursor for hard carbon and pure oxygen as the oxidant, adjusting the duration of high-temperature pure oxygen injection to achieve different degrees of oxidation crosslinking. They employed ex-situ XRD to investigate the influence of oxygen functional groups on the evolution of the carbon structure during the carbonization process. The C—O bonds were found to be in-plane, more inclined to participate in the formation of short-range graphite microcrystals. The interlayer C=O bonds decomposed during the heating process, generating gas and resulting in the formation of super-micropores and sectional closed pores. This also led to a decrease in planarity, forming a locally three-dimensional crosslinked structure, as illustrated in Fig. 8(a). Experimental results revealed that the introduction of oxygen functional groups in asphalt was crucial for achieving a completely random orientation of graphite microcrystals in hard carbon. Such hard carbon materials, containing ultrafine micropores and closed pores, provided excellent sodium storage sites and exhibited outstanding plateau capacity. In the low-voltage region (<0.06 V), the specific capacity increased from 95.35 to 132mAh g^{-1}, as shown in Fig. 8(b).

For oxygen-rich precursors, the pyrolysis process directly affects the introduction of oxygen functional groups. Liu and co-workers[120] devised the thermosetting reaction product of epoxy phenol–formaldehyde resin with maleic anhydride as the precursor for hard carbon. Since epoxy phenol–formaldehyde resin inherently contains abundant oxygen functional groups, the study systematically investigated the influence of

Please cite this article in press as: H. Zhang et al., Materials Today, (2025), https://doi.org/10.1016/j.mattod.2025.02.014

TABLE 1

The summary of doping mode and electrochemical performance for diverse heteroatom-doped hard carbon anodes.

Electrode materials	Methods	Heteroatoms content	Electrolyte	Binder	ICE	Rate performance: Reversible capacity (mAh g^{-1})/ Maximum current density(A g^{-1})	Cycle performance: Reversible capacity (mAh g^{-1})/ Cycle number/ Current density(A g^{1})	The specific functions and effects	Ref.
N-doped hard carbon	The precursor was mixed by sodium carbonate and hexamethylenetetramine (w/w = 1:1) before carbonization.	N content:7.9 wt %	1 M $NaClO_4$ in PC with 5 % FEC	PVDF	84.5 %	238 mAh g^{-1}/ 5 A g^{-1}	238 mAh g^{-1}/ 5000/5 A g^{-1}	Providing additional radical sites for Na^+; Contributing to the sodiation/ desodiation capacity for hard carbon in the plateau region.	[65]
N-doped hard carbon microspheres	NHCMs were constructed through amine–aldehyde polymerization with subsequent carbonization.	N content:4.6 wt %	1 M $NaPF_6$ in DEGDME	Sodium alginate	87 %	297 mAh g^{-1}/ 2 A g^{-1}	399 mAh g^{-1}/ 120/0.03 A g^{-1}	Introducing abundant defect sites for Na^+ adsorption and reducing the adsorption energy of hard carbon for Na^+. Reversible capacity is significantly increased during cycling.	[70]
N-doped hierarchical porous carbon networks (NHPCN)	Carbonation of $Ni_2(bim)_2(2\text{-}mim)_2$ under nitrogen atmosphere at different temperatures.	N content:15.3at %	0.8 M $NaPF_6$ in EC/DEC	PVDF	28 %	201.2 mAh g^{-1}/5 A g^{-1}	242.5 mAh g^{-1}/2500/1 A g^{-1}	Providing sufficient active interfacial sites and expanding the interlayer spacing. Facilitating electron transportation and enhancing Na^+ transport.	[74]
S-doped disordered carbon	DC-S samples were obtained by mixing NTCDA and sulfur at a mass ratio of 1:1, followed by calcination under N_2 atmosphere.	S content:26.9 wt %	1 M $NaPF_6$ in EC/DEC with 5 % FEC	PVDF	63.2 %	271 mAh g^{-1}/ 1 A g^{-1}	271 mAh g^{-1}/ 1000/1 A g^{-1}	Expanding interlayer distance and providing additional reaction sites. Facilitating the intercalation/extraction of Na^+ and increasing reversible capacity.	[66]
S-doped hard carbon	S-doped hard carbon (S-HC-p) and S-doped porous hard carbon (S-PHC-p) from pitch were synthesized through the molten salts method by using sulfur and $Na_2S_2O_3$ powders as S sources, respectively.	S content:6.3at %	1 M $NaClO_4$ in EC/DEC	PVDF	56 %	117 mAh g^{-1}/ 10 A g^{-1}	200 mAh g^{-1}/ 4000/1 A g^{-1}	Doping in the interlayers to expand the interlayer distance of the structure. The barrier energy of Na^+ diffusion is reduced and the rate performance is greatly improved.	[83]
S-doped carbon nanosheets	SOP and S powder were mixed at a mass ratio of 1:2, and annealed at 300⊠ for 2 h and 600⊠ for 3 h in Ar.	S content:15.5at %	1 M $NaClO_4$ in EC/DEC with 5 % FEC	PVDF	58 %	133 mAh g^{-1}/ 10 A g^{-1}	211 mAh g^{-1}/ 2000/5 A g^{-1}	Constructing 3D structural framework and expanding interlayer spacing. Providing sufficient active sites and promoting the insertion/extraction of Na^+.	[81]
P-doped hard carbon fibers	Electrospinning technology-carbonization.	P content:15 wt %	1 M $NaClO_4$ in PC with 2 % FEC	PVDF	61.5 %	134.6 mAh g^{-1}/1 A g^{-1}	386.4 mAh g^{-1}/100/0.02 A g^{-1}	Occupying the graphitic honeycomb lattice sites and promoting the generation of honeycomb structures. Increasing Na^+ diffusion pathways and enhancing Na^+ absorption.	[87]
P-doped hard carbon	The UPCs were prepared by pyrolyzing the mixture of PCl_3 and C_6H_{12}.	P content:30 wt %	1 M $NaClO_4$ in EC/DEC with 5 % FEC	PVDF	71.5 %	397 mAh g^{-1}/ 10 A g^{-1}	304.7 mAh g^{-1}/1500/1 A g^{-1}	Binding to surrounding C atoms to form protrusions in the carbon skeleton. Expanding interlayer spacing and enriching Na^+ adsorption sites.	[72]

(continued on next page)

Please cite this article in press as: H. Zhang et al., Materials Today, (2025), https://doi.org/10.1016/j.mattod.2025.02.014

TABLE 1 (*CONTINUED*)

Electrode materials	Methods	Heteroatoms content	Electrolyte	Binder	ICE	Rate performance: Reversible capacity (mAh g^{-1})/ Maximum current density(A g^{-1})	Cycle performance: Reversible capacity (mAh g^{-1})/ Cycle number/ Current density(A g^{1})	The specific functions and effects	Ref.
P-doped hard carbon	Petroleum and NaH_2PO_4 mixed powder were milled and then carbonized twice.	P content:2.77at %	1 M $NaPF_6$ in EC/DMC	Sodium alginate	80 %	145 mAh g^{-1}/ 3 A g^{-1}	145 mAh g^{-1}/ ~/3 A g^{-1}	Forming the specific heteroatom configurations and radicals. The sloping capacity and ICE are improved during charging and discharging processes.	[88]
B-doped hard carbon	H_3PO_4 was added to prepare aqueous GO suspension and dehydrated at 180 °C for 24 h, then pyrolyzed at 1100 °C for 5 h in Ar.	B content:5 wt %	1 M $NaPF_6$ in EC/DEC	PVDF	36.5 %	147 mAh g^{-1}/ 0.02 A g^{-1}	147 mAh g^{-1}/ 200/0.02 A g^{-1}	Taking place within the graphenic planes to increase in-plane local defects; The large first sodiation capacity is highly irreversible.	[89]
B-doped hard carbon nanospheres (BHCS)	BHCS were prepared by a combined hydrothermal polymerization and high temperature carbonization process with glucose and boric acid as the carbon and boron precursor.	B content:0.73at %	1 M $NaPF_6$ in EC/DEC	PVDF	65.4 %	80 mAh g^{-1}/2 A g^{-1}	180 mAh g^{-1}/ 400/0.1 A g^{-1}	Specific boron species (BC_3 and B–C–O) enlarge interlayer distance; Promote the diffusion dynamics of Na^+ between microcrystalline interlayers.	[68]
Zn-doped hard carbon	zinc (II) acetate was first coordinated with the $–NH_2–$ groups on 2,4-diaminophenol formaldehyde resin (DAFR) chains, then Zn-DAFR was pyrolyzed at 1300 °C in Ar.	Zn content:0.73 wt %	1 M $NaPF_6$ in DEGDME	PVDF	84 %	140 mAh g^{-1}/ 50 A g^{-1}	270.4 mAh g^{-1}/5000/2 A g^{-1}	Zn-N_4-C configuration decreases the dissociation energy (Ed) for P—F bond; Boost Na^+ to react with electron-rich F and form NaF compounds in SEI.	[69]
N/S co-doped Carbon	The as-prepared composite DBSA-doped and undoped cellulose/PANI microspheres and cellulose microspheres were pyrolyzed under following N_2 atmosphere at 400 ⊠ for 2 h and at 800 ⊠ for another 2 h, then were annealed.	N content:4.3 wt % S content:1.6 wt %	1 M $NaClO_4$ in EC/PC	PVDF	26.7 %	130 mAh g^{-1}/ 10 A g^{-1}	150 mAh g^{-1}/ 3400/0.5 A g^{-1}	Nitrogen doping enhances the electronic conductivity, S atoms enlarge the interlayer distances; Favor the adsorption of Na^+ and the fast sodium storage.	[96]
N/S co-doped porous hard carbon	Sucrose and trithiocyanuric acid (TA) were heated for cross-linking, then mixed with an excess amount of Teflon powder and further subject to a one-pot pyrolysis treatment.	N content:4.3at % S content:1.9at %	1 M $NaSO_3CF_3$ in DEGDME	CMC	84.9 %	277 mAh g^{-1}/ 5 A g^{-1}	273 mAh g^{-1}/ 1000/2 A g^{-1}	N, S co-doped porous hard carbon obtains relaxed interlayer distance, thin carbon shells, decent defect and dopant concentrations; Afford a superior capacity.	[109]
N, P co-doped carbon	Starch was used as precursor, urea and phytic acid act as cross-linking agents. Through calcination to obtain N, P co-doped carbon network.	N content:9.68at % P content:2.67at %	1 M $NaClO_4$ in EC/DEC with 2 % FEC	PVDF	42.6 %	119 mAh g^{-1}/ 5 A g^{-1}	119.1 mAh g^{-1}/2000/5 A g^{-1}	N, P co-doping adds many active sites, distorted carbon structures induce defects, and the graphite sheet layer spacing increases; Enrich the way for Na^+ to intercalate and adsorb.	[97]
N, P co-doped mesoporous hard carbon	The soybean roots were grinded into powder and carbonized under Ar atmosphere at 800 °C for 2 h.	N content:4.23at % P content:3.33at %	1 M $NaPF_6$ in EC/DEC	PVDF	44.4 %	179 mAh g^{-1}/ 5 A g^{-1}	160.3 mAh g^{-1}/2000/5 A g^{-1}	P has larger atomic size than N and higher electron donating ability, can modify the local charge density of carbon; N, P co-doping is essential for the enhanced Na^+ adsorption.	[99]

Please cite this article in press as: H. Zhang et al., Materials Today, (2025), https://doi.org/10.1016/j.mattod.2025.02.014

TABLE 1 (*CONTINUED*)

Electrode materials	**Methods**	**Heteroatoms content**	**Electrolyte**	**Binder**	**ICE**	**Rate performance: Reversible capacity (mAh g^{-1})/ Maximum current density(A g^{-1})**	**Cycle performance: Reversible capacity (mAh g^{-1})/ Cycle number/ Current density(A g^{1})**	**The specific functions and effects**	**Ref.**
N, B co-doped heteroatom carbon nanofibers (BNC NFs)	BNC NFs were synthesized via electrospinning and pyrolysis.	N content:5 wt % B content:1.1 wt %	1 M $NaPF_6$ in DEGDME	CMC	66.9 %	144 mAh g^{-1}/ 2 A g^{-1}	144 mAh g^{-1}/ 3000/2 A g^{-1}	N atom doping improves the wetting property, interlayer distance, pseudo-capacity, the B atom doping reduces the Fermi energy level and the lowest unoccupied molecular orbital of the material; Promote C to accept and absorb electrons from Na.	[104]
S, P co-doped hard carbon (P/SHCB)	The as-prepared P-HCB and sulfur powder were put into the tube furnace, heated up to 550 ⊠ for 2 h with a heating rate of 2 ⊠ min^{-1} in Ar.	S content:7.72 wt % P content:1.14 wt %	1 M $NaPF_6$ in DME	CMC	88.71 %	216 mAh g^{-1}/ 10 A g^{-1}	276 mAh g^{-1}/ 3000/10 A g^{-1}	S increases the interlayer spacing, P promotes the formation of C—S—P and P—O bonds to abundant structural defects and redox reaction sites; Contributes to the capacitive process under high rate.	[106]
N, S and P doped hierarchical vesicular carbon (HHVC)	Through a surface polymerization of HCCP and BPS on the ZIF-8, then the composite was carbonized.	S content:0.94 wt % P content:2.12 wt % N content:3.38 wt %	1 M $NaClO_4$ in PC	CMC	47.6 %	142.6 mAh g^{-1}/5 A g^{-1}	327.2 mAh g^{-1}/100/0.1 A g^{-1}	N, S, P doping enlarges interlayer spacing, enhances electronic conductivity, rapid mass transfer process; Obtain a high capacity.	[105]

Please cite this article in press as: H. Zhang et al., Materials Today, (2025), https://doi.org/10.1016/j.mattod.2025.02.014

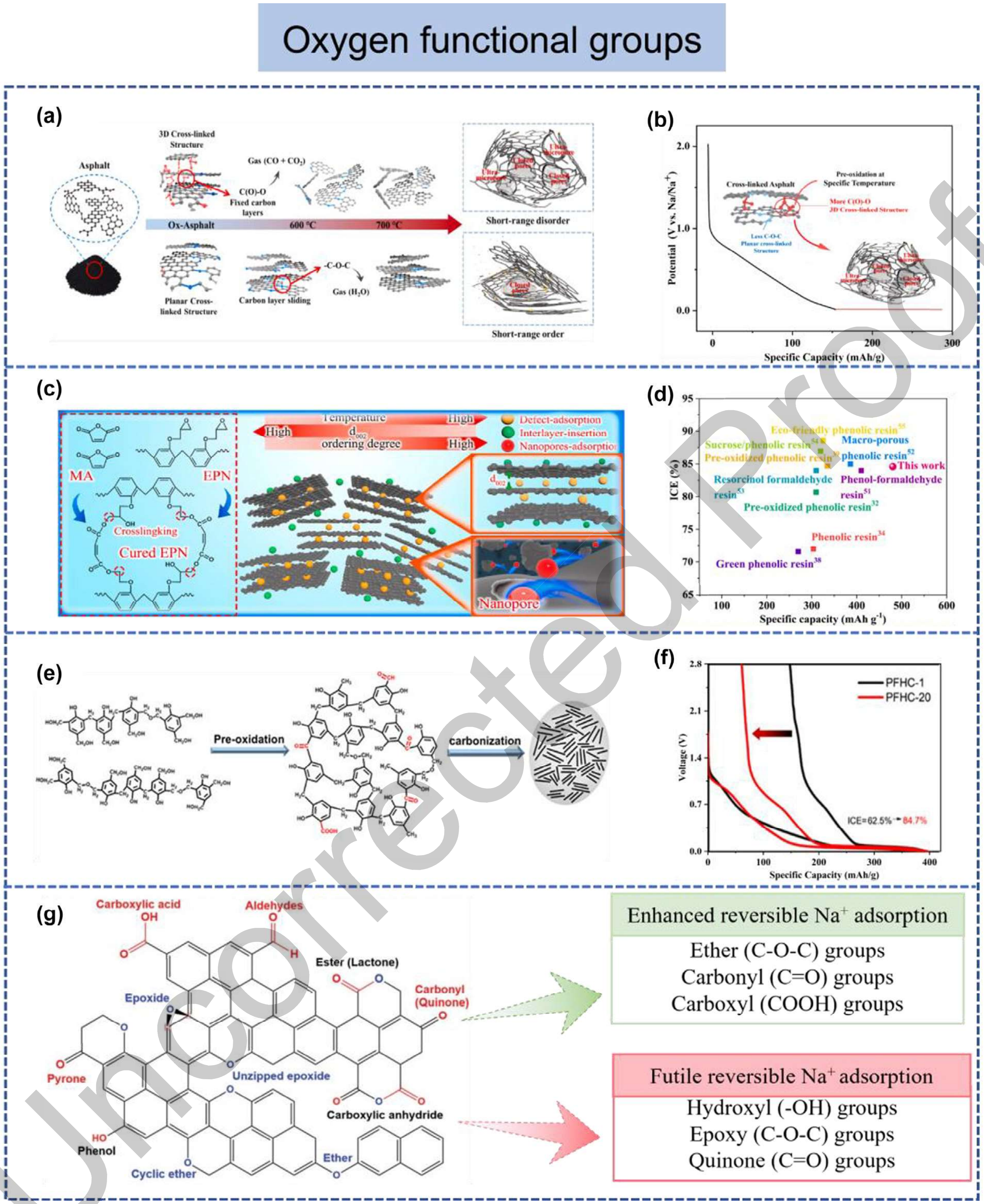

FIG. 8

(a) The effects of the oxygen functionalities on the evolution of carbon structure during carbonization. (b) The influence of carbon material microstructure on sodium storage during discharge. Reproduced with permission [119]. Copyright 2023, Elsevier. (c) Schematic diagram of the formation of polymer-based hard carbon by controlling pyrolysis temperature. (d) Comparisons of the specific capacity and initial columbic efficiency. Reproduced with permission [120]. Copyright 2023, Elsevier. (e) The illustration of modulating hard carbon anode microstructure by facile Pre-oxidation tactics. (f) The first charge–discharge curves of carbon materials with different degrees of peroxidation. Reproduced with permission [121]. Copyright 2021, American Chemical Society. (g) Typical oxygen-containing functional groups in carbon and its roles [22]. Copyright 2021, Royal Society of Chemistry.

pyrolysis temperature on the oxygen functional groups and electrochemical performance, as depicted in Fig. 8(c). Combined with Fourier-transform infrared spectroscopy (FTIR) and SAXS analysis, as the pyrolysis temperature increased, the interlayer spacing of hard carbon decreased, the nanopore radius increased, and the number of oxygen functional groups decreased. The rate

Please cite this article in press as: H. Zhang et al., Materials Today, (2025), https://doi.org/10.1016/j.mattod.2025.02.014

TABLE 2

The summary of oxygen functional group modulation of hard carbon anodes.

Electrode materials	Methods	Type of oxygen functional group/ Content	Electrolyte	Binder	ICE	Rate performance: Reversible capacity (mAh g^{-1})/ Maximum current density(A g^{-1})	Cycle performance: Reversible capacity (mAh g^{-1})/ Cycle number/ Current density(A g^{1})	Ref.
Bamboos derived hard carbon	Achieved regulation of its microstructure through carbonization temperature	C=O/4.64 at% C-O/3.22 at%	1 M NaPF$_6$ in DMG/ DME	CMC	84.1 %	206.5 mAh g^{-1}/2 A g^{-1}	295.9 mAh g^{-1}/500 /0.3 A g^{-1}	[62]
Polysaccharide-esterified starch (ES) derived hard carbon	A facile low-temperature hydrogen reduction strategy was proposed to regulate the oxygen content in ES	C=O/5.88 % C-O/17.4 %	1 M NaClO$_4$ in EC/DEC	PVDF	82.5 %	60 mAh g^{-1}/1 A g^{-1}	260 mAh g^{-1}/ 100 /0.1 A g^{-1}	[117]
Lignin-derived hard carbon	Heating the lignin spheres (LS) powders under an air atmosphere at different temperatures	C=O/2.42 %	MA-EN-EL-OSO216 in PC	SBR and CMC	45.6 %	32 mAh g^{-1}/5 A g^{-1}	150 mAh g^{-1}/ 400 /0.5 A g^{-1}	[118]
Hard carbons derived from the oxidized asphalts	Regulating the cross-linking time at specific temperature in pure O$_2$	C-O/67.0 at%	1 M NaClO$_4$ in EC/DEC	CMC	82.82 %	55 mAh g^{-1}/ 0.05 A g^{-1}	220 mAh g^{-1}/ 100/ 0.02 A g^{-1}	[119]
Epoxy phenol novolac resin derived hard carbon	Pyrolyzing at different temperature	C-O/∼ C=O/∼	1 M NaPF$_6$ in DME	Sodium alginate	84.6 %	170 mAh g^{-1}/4 A g^{-1}	389.2 mAh g^{-1}/1000/0.5 A g^{-1}	[120]
Phenol-formaldehyde resin derived hard carbon	Variable pre-oxidation time was designed to tune the cross-linking degree	C=O/72.83 %	1 M NaClO$_4$ in EC/DEC	CMC	84.7 %	75 mAh g^{-1}/1 A g^{-1}	196.9 mAh g^{-1}/300/0.1 A g^{-1}	[121]

performance deteriorated accordingly, indicating that the reduction of oxygen functional groups directly affected the rapid adsorption and desorption of sodium ions in the sloping segment. In comparison with other resin-based hard carbons, the utilization of oxygen-rich epoxy resin as a carbon precursor yielded hard carbon materials with the highest specific capacity of 480mAh g^{-1} and a prominent initial efficiency of 84.6 %, as shown in Fig. 8(d).

Shi et al. [121] employed a simple pre-oxidation strategy to treat phenol–formaldehyde resin precursor, as illustrated in Fig. 8(e). With the extending in pre-oxidation time, the crosslinking degree of precursor increased, impeding the ordered rearrangement of carbon atoms during the carbonization process. As a result, the obtained hard carbon exhibited a three-dimensional interconnected internal structure. XPS results reflected an enhancement in the C=O content from 59.5 % to 72.8 %, which provided more adsorption sites for sodium ions. In summary, pre-oxidation treatment promotes the crosslinking and oxidation of phenol–formaldehyde resin, resulting in hard carbon rich in carbonyl functional groups and a highly disordered internal structure. In Fig. 8(f), the ultimately pyrolyzed hard carbon owned the lowest specific surface area and demonstrated a higher initial efficiency of 84.7 %.

Fig. 8g exhibits the typical oxygen-containing functional groups present in hard carbon and elucidates their respective roles. The adsorption energies of sodium on hydroxyl (–OH) and epoxy (C-O-C) groups are both observed to be lower than the metal binding energy, suggesting that neither of these configurations enhances sodium adsorption effectively. Additionally, the adsorption energy of the quinone (C=O) group, which stands at −243 kJ/mol, surpasses the upper limit, necessitating a higher redox potential for desorption, thereby being deemed as irreversible adsorption. Conversely, the adsorption energies of ether (C-O-C), carbonyl (C=O), and carboxyl (COOH) groups lie within the range defined by the lower and upper limits, indicating their superior capacity for reversible adsorption [22,122,123]. Consequently, the precise incorporation of specific oxygen-containing functional groups into the carbon backbone is pivotal in improving the properties of hard carbon. Both oxygen-rich and pre-oxidation treatment precursors achieve the regulation of oxygen-containing functional groups in the hard carbon framework, especially the carbonyl group C=O. This modification enriches sodium storage sites and improves the dynamics of sodium ion transport [116]. Oxygen functional group engineering is a significant strategy for adjusting the surface chemical and electrochemical properties of hard carbon. Table 2 summarizes recent important works on oxygen functional group modulation of hard carbon anodes.

Surface coating

The low initial Coulombic efficiency (ICE) of hard carbon materials is the primary obstacle limiting their commercial applications. One method to enhance ICE is to reduce electrode interface defects, thereby minimizing side reactions and elec-

Please cite this article in press as: H. Zhang et al., Materials Today, (2025), https://doi.org/10.1016/j.mattod.2025.02.014

trolyte decomposition [124]. The interface contact between the electrode and electrolyte can be improved through surface coating or combining nanostructure materials with conductive materials, especially carbon-based materials. Through the rational design of the "interlayer", it is possible to alter the process of Na^+ desolvation on one hand and to shield excessive defects on the surface of hard carbon, thereby suppressing the continuous degradation of electrolytes. Ultimately, surface coating modification is achieved to adapt to different electrolytes while ensuring excellent electrochemical performance. General improvement strategies include coating with nanoscale molecular sieves [125], alumina [126] and a soft carbon layer [127].

In order to regulate the transport process of Na^+ at the interface, Yang et al. [125] proposed a stepwise desolvation strategy by preparing a 3Å zeolite molecular sieve membrane tightly adhered to the surface of hard carbon. This approach transformed the direct desolvation on the hard carbon negative electrode into stepwise desolvation, which enhanced the rate capability and stability of sodium storage in esters and ethers. Stepwise desolvation allowed the concentration of the electrolyte to form a more densely packed electrolyte. It promoted the formation of a thin and predominantly inorganic solid electrolyte interface (SEI), reducing the activation energy for Na^+ transport through the SEI, as shown in Fig. 9(a). Therefore, the synergistic improvement in Na^+ transport dynamics imparted excellent rate performance and cycling stability. With raising current density, the proportion of platform capacity significantly increased. During extended cycling, a platform capacity proportion as high as 73 % could be maintained at a current density of 0.1 A g^{-1}. Moreover, Cao et al. [126] designed a strategy using atomic layer deposition to deposit an ultra-thin Al_2O_3 film on the surface of the hard carbon anode. Experimental results revealed that the Al_2O_3 film deposited on the hard carbon surface served as an "artificial solid electrolyte interface (SEI)," effectively suppressing electrolyte decomposition, thereby enhancing the initial Coulombic efficiency and improving cycling stability. Simultaneously, the surface-deposited ultra-thin Al_2O_3 film effectively reduced interfacial resistance and electrode overpotential, which improved the reversible specific capacity in Fig. 9(b).

Besides the ionic conduction between the interface, the intrinsic electronic conduction properties of hard carbon materials are also key design factors. Xu and co-workers[128] chose asphalt as the coating source and employed chemical vapor-phase deposition to construct an asphalt-based soft carbon coating layer on the surface of coal-based hard carbon. This process reduced surface defects in coal-based hard carbon, meanwhile enhanced their structural stability and conductivity. Furthermore, the oxygen-containing volatiles in asphalt undergo cross-linking reactions with the oxygen-containing functional groups in coal molecules, facilitating the thermal stability of coal-based molecular chains. Which results in an increased proportion of quasi-graphite phases in the microcrystalline structure of the carbonization product, these structures contributed to extend interlayer sodium storage capacity in the plateau region.

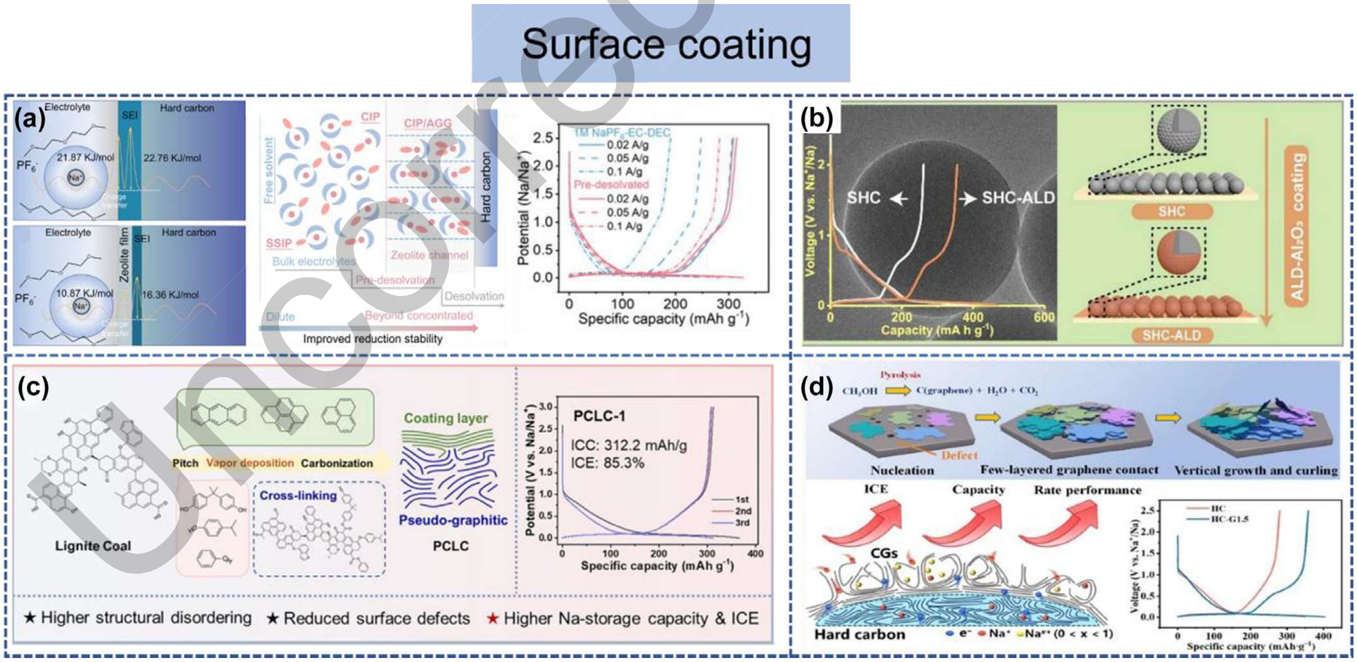

FIG. 9

(a) Comparison of the kinetics of desolvation, Na^+ transport through the SEI and electrochemical performance in pristine ether electrolytes and predesolvated electrolytes. Reproduced with permission [125]. Copyright 2022, PNAS. (b) Al_2O_3 coated composite hard carbon nanospheres and charge–discharge performance. Reproduced with permission [126]. Copyright 2019, Elsevier. (c) The schematic diagram for the fabrication of coal-derived carbons coated with pitch-derived soft carbon and charge/discharge profiles of first three laps. Reproduced with permission [128]. Copyright 2023, Elsevier. (d) The schematic illustration of the growth process of curled graphene coated on hard carbon surface and improvement of electrochemical performance. Reproduced with permission [129]. Copyright 2023, Springer.

Please cite this article in press as: H. Zhang et al., Materials Today, (2025), https://doi.org/10.1016/j.mattod.2025.02.014

TABLE 3

The summary functionalized design works on hard carbon surface coating.

Electrode materials	Methods	Medium	Electrolyte	Binder	ICE	Rate performance: Reversible capacity(mAh g^{-1})/ Maximum current density(A g^{-1})	Cycle performance: Reversible capacity (mAh g^{-1})/ Cycle number/ Current density(A g^{1})	Ref
HC-Al_2O_3	Coating amorphous Al_2O_3 layers on the surface of disordered amorphous HC	Al_2O_3	1 M $NaPF_6$ in EC/DEC	PVDF	81.1 %	77.9 mAh g^{-1}/1 A g^{-1}	80 mAh g^{-1}/ 2000/1 A g^{-1}	[63]
Hard carbon with a 3A zeolite molecular sieves coating	The zeolite powder was mixed with PVDF with a ratio of 9:1 using NMP as solvent, which was homogeneously coated onto a glass plate by scraper	3A zeolite molecular sieves	1 M $NaPF_6$ in PC/FEC	Sodium alginate	95.4 %	224 mAh g^{-1}/ 5 A g^{-1}	251.9 mAh g^{-1}/ 4500 /1 A g^{-1}	[125]
Al_2O_3-coated hard carbon	Trimethylaluminum (TMA) and deionized water were used as precursors in the ALD-Al_2O_3 deposition process with a growth temperature at 200 °C	Al_2O_3	1 M $NaClO_4$ in EC/DEC	Polyacrylic acid	75 %	/	291.4 mAh g^{-1}/ 50 /0.05 A g^{-1}	[126]
Coal-based carbons coated by pitch derived soft carbon (PCLC)	Vapor deposition: heating treatment at 400 ○C for volatile pitch-derived species can deposit on the surface, then carbonized at 1200 ○C	Pitch-based soft carbon layer	1 M $NaClO_4$ in EC/DEC with 5 % FEC	CMC	85.3 %	106.1 mAh g^{-1}/1 A g^{-1}	230.5 mAh g^{-1}/ 1000/0.3 A g^{-1}	[128]
Growing curly graphene sheets (CGs) on the surface of HC (HC-CGs)	Thermal CVD without other carrier gases (such as argon and hydrogen) and catalysts	Curly graphene sheets (CGs)	1 M $NaPF_6$ in DEGDME	PVDF	89.3 %	145.8 mAh g^{-1}/5 A g^{-1}	283.5 mAh g^{-1}/ 650/0.3 A g^{-1}	[129]
Hard carbon with a soft-carbon coating	Impregnate the pitch into both the surface and the internal pores of commercial paper towels followed by an annealing process at 1200 and 1400 °C	Soft-carbon	1 M $NaPF_6$ in EC/DMC	PVDF	94.1 %	122.9 mAh g^{-1}/0.5 A g^{-1}	290 mAh g^{-1}/ 100/0.02 A g^{-1}	[131]
Perylene (PER) and terephthaloyl chloride (TPC) derived HC	Adjusting the feeding ration of perylene (PER) to terephthaloyl chloride (TPC)	Soft-carbon	1 M $NaClO_4$ in EC/PC with 5 % FEC	PVDF	75 %	50 mAh g^{-1}/10 A g^{-1}	82 mAh g^{-1}/ 8000/1 A g^{-1}	[134]

Please cite this article in press as: H. Zhang et al., Materials Today, (2025), https://doi.org/10.1016/j.mattod.2025.02.014

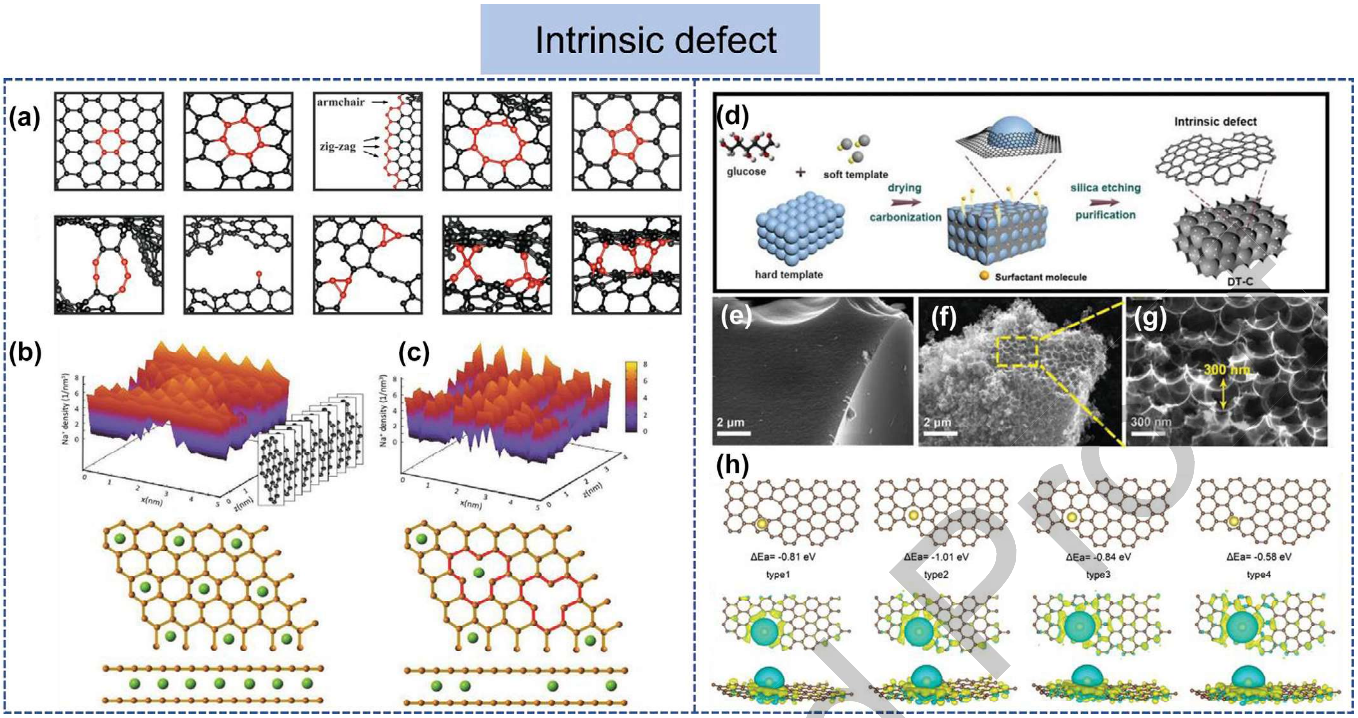

FIG. 10

(a) The schematics of representative structural motifs in HC. Reproduced with permission [40]. Copyright 2022, Wiley-VCH. (b) Na^+ distribution in a vacancy defect free electrode. (c) Na^+ distribution in the presence of vacancy defects in the graphitic layers. Reproduced with permission [138]. Copyright 2018, Wiley-VCH. (d) The schematic illustrations of synthesis process of intrinsic defect hard carbon by hard templates. (e) SEM image of hard carbon microstructure. (f, g) The porous structures and interconnected framework of hard carbon. (h) Theoretical simulations based on Na atom absorbed on the carbon structures with di-vacancy defects (type1, type2, type3) and single vacancy defects. Reproduced with permission [139]. Copyright 2020, Wiley-VCH.

Ultimately, at a current density of 0.03 A g^{-1}, the first Coulombic efficiency reached 85.3 %, with a reversible capacity of 312mAh g^{-1} as depicted in Fig. 9(c).

Through a low-pressure CVD method, Xie et al. [129] achieved the in-situ growth of a modified layer composed of curled graphene on the surface of hard carbon. The curled graphene on the surface not only improved the electronic/ion conductivity of hard carbon but also effectively shielded its surface defects, optimizing its Coulombic efficiency. Due to the spontaneously curled structure of curled graphene (CG), the formed micropores (≤2 nm) provide additional active sites, which increased its specific capacity in Fig. 9(d). With a comparable effect, Xu Bin et al. [130] modified the molecular structure of phenolic resin by incorporating sucrose, thereby creating an intertwined phenolic resin/sucrose (PF/S) chemical polymer network. After carbonization, this resulted in an amorphous hard carbon material with distinct pseudo-graphitic regions. The resultant material exhibited reduced surface defects, enhanced electronic conductivity, and robust structural stability, ultimately contributing to a prolonged cycle life.

By combining hard carbon with inactive materials towards sodium ions, such as soft carbon, graphite and Al_2O_3 etc, the direct contact between the hard carbon anode and the electrolyte can be diminished [131]. These measures prevent undesired reactions in the electrode–electrolyte interface, thereby influencing the formation of the solid electrolyte interface (SEI) and ameliorating reaction kinetics [132,133]. Applying surface coatings or integrating nanostructured materials with hard carbon frequently necessitates methodologies like chemical vapor deposition (CVD) and atomic layer deposition (ALD). These techniques generally entail high precision and intricate processing steps, consequently elevating the expenses associated with modifying hard carbon [125]. Hence, there is an urgent need for the advancement of more economical coating technologies. As mentioned approaches demonstrate theoretical support for the precise structural modulation of the hard carbon anode surface. The summary of functionalized design works on hard carbon surface coating is presented in Table 3.

Intrinsic defect

The disordered microcrystalline graphene nanosheets constituting hard carbon exhibit numerous defects [135]. As mentioned earlier, external defects caused by the introduction of heteroatoms and oxygen-containing functional groups into the carbon framework typically occur at vacancies and edges [64,136]. Another type of defect is intrinsic, primarily composed of dangling bonds and sp^3-hybridized carbons branched with other structures, including vacancies and pores on the nanosheets [137]. These inherent defects, such as pentagons, heptagons, octagons, and their combinations with various non-hexagonal structures, lead to the curvature of graphene nanosheets, as shown in Fig. 10(a) [40]. The presence of these defects directly impinges sodium "adsorption-insertion-filling" sites, thereby altering sodium storage capacity.

Cao and co-workers[138] controlled the carbonization temperature to adjust the internal defects in the structure of hard car-

Please cite this article in press as: H. Zhang et al., Materials Today, (2025), https://doi.org/10.1016/j.mattod.2025.02.014

TABLE 4

The summary of research progress achieved in the meticulous regulation of intrinsic defects in hard carbon.

Electrode materials	Research scheme	Electrolyte	Binder	ICE	Rate performance: Reversible capacity(mAh g^{-1})/ Maximum current density (A g^{-1})	Cycle performance: Reversible capacity (mAh g^{-1})/ Cycle number/ Current density(A g^{1})	Ref.
Flexible natural paper towels fabricated hard carbon	Utilize a metal ions-catalyzed pyrolysis of flexible paper towels to prepare hard carbon anodes	1 M NaPF$_6$ in EC/DEC	/	92.05 %	48 mAh g^{-1}/0.5 A g^{-1}	320 mAh g^{-1}/ 200/0.02 A g^{-1}	[37]
Sucrose derived hard carbon	Tune synthesis temperature and use molecular dynamics simulate sintering method to create HC structural model	1 M NaPF$_6$ in BASF	PVDF	68 %	/	278 mAh g^{-1}/ ~/0.03 A g^{-1}	[40]
Mixture of sucrose and phenol formaldehyde resin fabricated hard carbon	Pyrolysis of the mixture of sucrose and phenol formaldehyde resin, then use organic molecule vapors to reduce defects	0.8 M NaPF$_6$ in EC/DMC	PVDF	85 %	/	310 mAh g^{-1}/ 100/0.02 A g^{-1}	[137]
Sucrose derived hard carbon	Modulate different heating rate and use classical density functional theory coupled with Poisson–Nernst–Planck drift diffusion formalism to simulate Na$^+$ diffusion	1 M NaClO$_4$ in EC/DEC	PAA	86.1 %	/	361 mAh g^{-1}/ 100/0.02 A g^{-1}	[138]
Glucose as hard carbon sources	Use template-assisted methods to expose more intrinsic defects during the synthesis of carbon materials and simulate by DFT calculation	1 M NaClO$_4$ in EC/DEC with 5 % FEC	PVDF	61.2 %	156 mAh g^{-1}/ 10 A g^{-1}	153 mAh g^{-1}/ 5000/10 A g^{-1}	[139]
Mixture of magnesium gluconate and glucose derived hard carbon	Heat a freeze-dried mixture of magnesium gluconate and glucose by a MgO-template technique	1 M NaPF$_6$ in EC/DEC	Sodium polyacrylate	88 %	370 mAh g^{-1}/ 2.5 A g^{-1}	478 mAh g^{-1}/ 35/0.025 A g^{-1}	[140]
Cellulose based hard carbon	Pyrolysis of cellulose, then modified with concentrated nitric acid and half of the HC-oxidized carbon is heat under hydrogen	1 M NaPF$_6$ in EC/DMC	PVDF	82.7 %	/	310 mAh g^{-1}/ ~/0.0372 A g^{-1}	[141]
Benzene as the carbon precursor and Activated carbon as the substrate	The facile space-confined chemical vapor deposition (SC-CVD) strategy to fill graphitic-like carbon domains into the slit micropores of AC to obtain FC (Filling carbon)	1 M NaPF$_6$ in DEGDME	PAA	88.4 %	190 mAh g^{-1}/2 A g^{-1}	284 mAh g^{-1}/ 1000/0.5 A g^{-1}	[145]

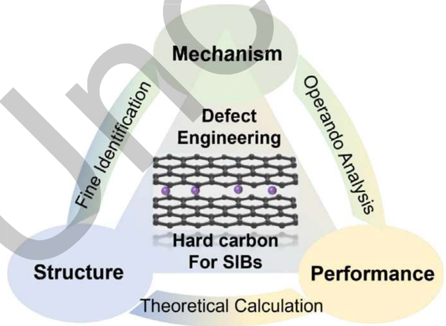

FIG. 11

Conducting defect engineering design of hard carbon anodes around the "mechanism-structure-performance" relationship.

bon materials. To elucidate how defects in the carbon layer affect Na$^+$ storage, theoretical calculations were performed by constructing models. It was found that in a defect-free structure, Na$^+$ predominantly occupied most available sites, as depicted in Fig. 10(b). In the presence of defects in the carbon layer, the distribution of Na$^+$ became sparse, with many sites remaining unoccupied. Defective sites on the graphite basal plane captured Na$^+$ strongly due to adsorption energy, trapping them in the plane. These captured Na$^+$ generated a repulsive electric field against other ions, reducing the concentration of Na$^+$ between the graphite layers. Ultimately, the intrinsic defects affected the migration and diffusion barriers of Na$^+$ in the graphite microcrystals, as shown in Fig. 10(c). Cao suggested that an excessive number of intrinsic defects in the graphite layers could reduce the effective sodium storage capacity of the hard carbon anode.

Template assistance is another significant method of controllably regulating internal defects in hard carbon. Yang et al. [139] employed glucose as a carbon source and utilized a template-assisted method to prepare hard carbon materials with more intrinsic defects, as illustrated in Fig. 10(d). In contrast to the regular surface of hard carbon shown in Fig. 10(e), Fig. 10(f-g) pre-

Please cite this article in press as: H. Zhang et al., Materials Today, (2025), https://doi.org/10.1016/j.mattod.2025.02.014

sented a honeycomb-like structure with pores approximately 300 nm in diameter. This interconnected honeycomb structure shortened the distance for Na^+ transport, facilitating Na^+ storage. Electrochemical performance tests revealed a positive correlation between the adsorption behavior of Na^+ on the carbon material and the intrinsic defect ratio. Additionally, density functional theory (DFT) calculations demonstrated that compared to the adsorption energy of Na^+ on pristine graphene (0.22 eV), the corresponding ΔEa values for four different defects were −0.81, −1.01, −0.84, and −0.58 eV, respectively. The hard carbon model introduced with intrinsic defects exhibited higher Na^+ adsorption capacity, as depicted in Fig. 10(h). Yang confirmed that the presence of intrinsic defects indeed favored the adsorption of Na^+ on hard carbon, highlighting the crucial role of introducing intrinsic carbon defects in enhancing sodium storage performance.

In conclusion, increasing defect concentration is a “Double-edged Sword”. One hand, the elevation of defect concentration furnishes more adsorption and sodium storage sites, ameliorating diffusion pathways with lower barriers for solid-phase Na^+ transport [140,141]. Moreover, the increased defects on pore walls could reduce the average transfer charge of sodium clusters, weakening the metallic properties of sodium clusters and facilitating their rapid formation at higher potentials [134,142]. Conversely, numerous defects create irreversible sodium adsorption sites, serving as a contributor to irreversible capacity, ultimately leading to a decrease in ICE. Therefore, future research efforts should aim to clarify the reversibility of sodium adsorption on different types of defects, selectively increase defect concentrations, and strike a balance between enhancing capacity, rate capability, and optimizing ICE [143,144]. Table 4 summarizes the research progress achieved in the meticulous regulation of intrinsic defects in hard carbon.

Conclusion and perspective

Defect engineering design in hard carbon materials has always been a focal point in the research of the anode side of SIBs. Based on different sodium storage mechanisms, it can be refined as follows: 1) Introducing heteroatoms or defects into the carbon lattice to induce capacitive adsorption or reactions [70]. 2) Expanding the interlayer distance of graphite to promote the insertion of Na^+ [35]. 3) Optimizing pore networks to facilitate the transport or storage of Na^+ [146]. 4) Constructing well-defined 3D channels, carbon morphologies and frameworks to shorten the ion/electron transfer length [147]. 5) Surface engineering to optimize its physicochemical properties [145]. Fine-tuning of the structure could be achieved through heteroatom doping, introduction of oxygen functional groups, and surface coating, guided by sodium storage mechanisms. The specific criteria for defect engineering implementation are illustrated in Fig. 11. Further research on the relationship between regulated structure, sodium storage mechanisms, and performance requires more effective fine identification, operando analysis, and theoretical calculations.

Building upon the aforementioned design criteria, this review systematically summarizes the effectiveness of single and multi-doping of N, S, P, B, and Zn to introduce heterogeneous defects, which enhance the materials' reversible capacitive adsorption of Na^+. Ultimately, the slope capacity is improved, which also directly impacts rate performance of hard carbon materials. It highlights the reduction of surface defects and enhancement of initial performance through surface coating. The introduction of oxygen functional groups and the modulation of intrinsic defects using a template method to improve sodium storage performance are also discussed. Additionally, the review summarizes studies related to theoretical calculations to analyze in detail the impact of various optimization methods on the local electronic structure of hard carbon, revealing the fundamental reasons for the improvement in sodium storage performance. In-situ analysis of dynamic electrochemical processes is crucial for a better understanding of sodium storage under realistic conditions. In summary, a profound understanding of the mechanism-structure-performance relationship can lead to the rational design of ideal hard carbon materials, opening the door to high-performance sodium-ion battery energy storage system applications.

So far, researchers have only conducted detailed studies on a limited number of doping elements [33], leaving many other doping elements worth further exploration in SIBs. Additionally, surface defects (both internal and external) provide active centers for charge storage but also induce irreversible reactions. Therefore, minimizing side reactions while preserving the additional charge storage capacity brought by defects is a key challenge. There is limited research on the defects causing side reactions, resulting in a lack of clarity on the specific defect types responsible for severe electrolyte reactions. In short characterizing and analyzing side reactions induced by defects should be emphasized. Protecting defects is a viable approach that can minimize side reactions without compromising the overall capacity.

Herein, the summary of defect engineering provides a robust theoretical foundation and technical support for the future commercial application of hard carbon anodes in SIBs, contributing to the industrialization process. Future research on the practical utilization of hard carbon anodes in SIBs should focus on the following aspects:

1. Understanding structure–property relationships: Gain a deep understanding of the structure-performance relationship between carbon materials and sodium clusters to reduce the energy barriers of sodium clusters and enhance the safety of carbon anodes, aiming for carbon anode designs that combine high specific capacity and safety [49].
2. Reaction kinetics of sodium clusters: Address the slow reaction kinetics of sodium clusters at low potential platforms, a critical bottleneck for practical applications [148]. Future work should emphasize the study of the kinetic behavior during the platform stage.
3. Material design at the cell level: Consider material design from the perspective of the entire cell, including factors such as compaction density, electrode thickness, slurry characteristics, and optimize initial Coulombic efficiency. Additionally, focus on the compatibility with the cathode, systematically improving the performance of hard carbon anodes [149].

Please cite this article in press as: H. Zhang et al., Materials Today, (2025), https://doi.org/10.1016/j.mattod.2025.02.014

4. Suitability of electrolyte systems: As a crucial reaction medium in battery systems, the electrolyte significantly impacts battery performance. Such as compared to ester-based electrolyte systems, the desolvation barrier of Na$^+$ in ether-based electrolytes is significantly lower, at less than one-third of that in ester-based electrolytes, which facilitates the formation of a thin and stable SEI film [150]. Therefore, further investigation into its mechanisms through a combination of electrochemistry, diffusion kinetics, and first-principles studies is necessary to provide guidance for the formulation of high-performance electrolyte systems.
5. Cost control and pyrolysis process selection: The cost of hard carbon materials remains one of the key bottlenecks limiting their commercialization. Therefore, selecting sustainable, environmentally friendly, and low-cost carbon sources while maintaining electrochemical performance is a pressing issue [151]. Additionally, traditional pyrolysis processes are often complex, time-consuming, and energy-intensive. Emerging sintering technologies, such as multi-field-regulated spark plasma sintering (SPS) and Joule heating sintering, offer promising pathways for the rapid and high-throughput synthesis of hard carbon materials [152,153].

CRediT authorship contribution statement

Haihan Zhang: Writing – original draft. **Siyuan Lin:** Writing – original draft. **Chengyong Shu:** Writing – review & editing, Methodology. **Zexun Tang:** Methodology, Investigation. **Xiaowei Wang:** Writing – review & editing. **Yuping Wu:** Writing – review & editing, Supervision, Investigation. **Wei Tang:** Writing – review & editing, Supervision, Investigation, Funding acquisition, Conceptualization.

Data availability

Data will be made available on request.

Declaration of competing interest

The authors declare that they have no known competing financial interests or personal relationships that could have appeared to influence the work reported in this paper.

Acknowledgement

The project was support by the National Key R&D Program of China (2021YFB2400400), the National Natural Science Foundation of China (Grant No. 22379120), the Key Research and Development Plan of Shanxi Province (China, Grant No.2021-JLM-36), "Young Talent Support Plan" of Xi'an Jiaotong University (71211201010723), "Young Talent Support Plan" of Xi'an Jiaotong University (HG6J003), "1000-Plan program" of Shaanxi Province and the Higher Education Institution Academic Discipline Innovation and Talent Introduction Plan ("111 Plan") (No.B23025).

References

[1] R. Usiskin et al., Nat. Rev. Mater. 6 (11) (2021) 1020.
[2] H. Kang et al., J. Mater. Chem. A 3 (35) (2015) 17899.
[3] D. Chen et al., Energy Environ. Sci. 14 (4) (2021) 2244.
[4] J.Y. Hwang et al., Chem Soc Rev 46 (12) (2017) 3529.
[5] M. Zhang et al., Nano Energy 82 (2021) 105738.
[6] Y. Yang et al., Adv. Funct. Mater. (2023) 2302277.
[7] Y. Wan et al., Nano Mater. Sci. 5 (2) (2023) 189.
[8] Y. Chen et al., Mater. Today 73 (2024) 260.
[9] S. Li et al., Mater. Today 72 (2024) 207.
[10] C. Lu et al., Adv. Energy Mater. 14 (27) (2024) 2401221.
[11] X. Dou et al., Mater. Today 23 (2019) 87.
[12] T. Liu et al., Energy Environ. Sci. 12 (5) (2019) 1512.
[13] L. Xie et al., Adv. Energy Mater. 11 (38) (2021) 2101650.
[14] D. Alvira et al., Chem. Eng. J. 447 (2022) 137468.
[15] Q. Wei et al., Energy Environ. Mater. 3 (3) (2020) 221.
[16] G. Li et al., Energy Mater. 2 (3) (2022) 200020.
[17] Y.-F. Sun et al., Energy Mater. 4 (1) (2024) 400002.
[18] Y. Chu et al., Adv Mater 35 (31) (2023) e2212186.
[19] S. Zhao et al., Small 17 (48) (2021) e2007431.
[20] Z. Liu et al., ACS Cent. Sci. 9 (6) (2023) 1076.
[21] Y. Fang et al., Matter 1 (1) (2019) 90.
[22] X. Feng et al., Energy Environ. Sci. 14 (4) (2021) 2036.
[23] J. Zhang et al., Cell Rep. Phys. Sci. 3 (5) (2022) 100868.
[24] D. Saurel et al., Adv. Energy Mater. 8 (17) (2018) 1703268.
[25] H. Cheng et al., ACS Energy Lett. 7 (1) (2022) 490.
[26] L. Liu et al., Research 6 (2023) 0209.
[27] F. Xie et al., Prog. Energy 2 (4) (2020) 042002.
[28] G. Wang et al., Chem Soc Rev 50 (4) (2021) 2388.
[29] W. Chen et al., Small Methods 3 (4) (2018) 1800323.
[30] X. Chen et al., Carbon Energy 4 (6) (2022) 1133.
[31] N. Sun et al., Adv. Energy Mater. 12 (27) (2022) 2200715.
[32] L.F. Zhao et al., Adv. Energy Mater. 11 (1) (2020) 2002704.
[33] M. Liu et al., Adv. Funct. Mater. 32 (31) (2022) 2203117.
[34] X. Yu et al., Mater. Today 59 (2022) 25.
[35] M. Yuan et al., Chem. Mater. 34 (7) (2022) 3489.
[36] Q. Li et al., Natl Sci Rev 9 (8) (2022) nwac084.
[37] J. Zhao et al., Adv. Energy Mater. 13 (18) (2023) 2300444.
[38] Y. Yang et al., J. Mater. Chem. A 11 (6) (2023) 2947.
[39] Y. Zhao et al., Small (2023) e2303296.
[40] T.W. Surta et al., Adv. Energy Mater. 12 (25) (2022) 2200647.
[41] R.E. Franklin, Proc. r. Soc. Lond. A 209 (1097) (1951) 196.
[42] L.L. Ban et al., J. Appl. Crystallogr. 8 (4) (1975) 415.
[43] S.J. Townsend et al., Phys. Rev. Lett. 69 (6) (1992) 921.
[44] P.J.F. Harris et al., Philos. Mag. A 76 (3) (1997) 667.
[45] A.P. Terzyk et al., Phys. Chem. Chem. Phys. 9 (44) (2007) 5919.
[46] D.J.R. Stevens D A, J. Electrochem. Soc. 147 (4) (2000) 1271.
[47] C. Bommier et al., Nano Lett 15 (9) (2015) 5888.
[48] H. Kim et al., Adv Mater 35 (12) (2023) e2209128.
[49] L. Kitsu Iglesias et al., Adv. Energy Mater. 13 (44) (2023) 2302171.
[50] P. Bai et al., Adv. Energy Mater. 8 (15) (2018) 1703217.
[51] Z.L. Yu et al., J. Am. Chem. Soc. 138 (45) (2016) 14915.
[52] Y. Aniskevich et al., Adv. Energy Mater. 14 (18) (2024) 2304300.
[53] Y. Morikawa et al., Adv. Energy Mater. 10 (3) (2019) 1903176.
[54] S. Qiu et al., Adv. Energy Mater. 7 (17) (2017) 1700403.
[55] N. Sun et al., Adv. Energy Mater. 9 (32) (2019) 1901351.
[56] Z. Wang et al., Adv. Energy Mater. 11 (11) (2021) 2003854.
[57] Q. Li et al., Adv. Energy Mater. 12 (37) (2022) 2201734.
[58] S. Alvin et al., Carbon 145 (2019) 67.
[59] X. Chen et al., Adv. Energy Mater. 12 (24) (2022) 2200886.
[60] H. Au et al., Energy Environ. Sci. 13 (10) (2020) 3469.
[61] Z. Song et al., Chem. Eng. J. 470 (2023) 144237.
[62] T. Xu et al., Chem. Eng. J. 452 (2023) 139514.
[63] C.X. Yu et al., Carbon Energy 5 (1) (2023) e220.
[64] Y. Zhang et al., Adv. Mater. 32 (7) (2020) 1905923.
[65] Q. Gan et al., Small Methods 5 (9) (2021) 2100580.
[66] W. Li et al., Energy Environ. Sci. 8 (10) (2015) 2916.
[67] W. Song et al., J. Alloys Compd. 946 (2023) 169384.
[68] D. Wu et al., J. Mater. Chem. A 10 (33) (2022) 17225.
[69] Z. Lu et al., Adv. Mater. 35 (26) (2023) e2211461.
[70] R. Chen et al., Small 19 (44) (2023) 2303790.
[71] C. Sun et al., Energy Environ. Mater. 6 (2023) e12603.
[72] J. Yan et al., Adv. Energy Mater. 11 (21) (2021) 2003911.
[73] J. Zhou et al., Energy Storage Mater. 46 (2022) 20.
[74] D. Su et al., Nano Res. 13 (10) (2020) 2862.
[75] M. Yang et al., Carbon 176 (2021) 71.
[76] U. Ghani et al., ACS Appl. Mater Interfaces 14 (42) (2022) 47507.
[77] G. Huang et al., ChemSusChem 15 (20) (2022) e202201310.
[78] G. Huang et al., ChemSusChem 16 (7) (2023) e202202070.
[79] K. Ramachandran et al., Rare Met. 41 (7) (2022) 2481.

Please cite this article in press as: H. Zhang et al., Materials Today, (2025), https://doi.org/10.1016/j.mattod.2025.02.014

[80] G. Shi et al., ChemElectroChem 9 (8) (2022) e202200138.
[81] G. Zhao et al., Nano Energy 67 (2020) 104219.
[82] Q. Jin et al., Energy Storage Mater. 27 (2020) 43.
[83] Z. Hong et al., Adv. Mater. 30 (29) (2018) 1802035.
[84] W. Liu et al., ACS Nano 14 (1) (2019) 974.
[85] G.-H. Lee et al., J. Mater. Chem. A 10 (31) (2022) 16506.
[86] X. Wang et al., ACS Appl. Mater Interfaces 13 (10) (2021) 12059.
[87] Y. Li et al., Adv. Energy Mater. 8 (18) (2018) 1702781.
[88] F. Xie et al., Angew. Chem. Int. Ed. 61 (11) (2022) e202116394.
[89] Z. Li et al., Adv. Energy Mater. 7 (18) (2017) 1602894.
[90] J. Zhang et al., Energy Fuels 37 (3) (2023) 2379.
[91] Q. Zhao et al., Inorg. Chem. Front. 10 (9) (2023) 2574.
[92] H. Zhang et al., Energy Fuels 37 (19) (2023) 15127.
[93] H. Zhang et al., Adv. Funct. Mater. 33 (34) (2023) 2300769.
[94] Z. Huang et al., J. Energy Storage 72 (2023) 108406.
[95] X. Chen et al., J. Energy Chem. 77 (2023) 338.
[96] D. Xu et al., Adv. Energy Mater. 6 (6) (2016) 1501929.
[97] C. Chen et al., Carbon 170 (2020) 225.
[98] M. Yang et al., Carbon Energy 4 (1) (2021) 45.
[99] S. Tao et al., Carbon 178 (2021) 233.
[100] H. Wang et al., Carbon 165 (2020) 204.
[101] W. Xu et al., J. Power Sources 442 (2019) 227184.
[102] S. Wu et al., Batteries Supercaps 6 (1) (2022) e202200427.
[103] S. Wu et al., Carbon 218 (2024) 118756.
[104] I. Jeon et al., Electrochim. Acta 439 (2023) 141730.
[105] G. Zou et al., Adv. Sci. 5 (7) (2018) 1800241.
[106] Z. Wang et al., J. Alloys Compd. 911 (2022) 164979.
[107] C. Chen et al., J. Energy Chem. 54 (2021) 482.
[108] W. Shao et al., J. Mater. Chem. A 7 (11) (2019) 6363.
[109] Z. Pei et al., Energy Storage Mater. 28 (2020) 55.
[110] X. Jin et al., Small 18 (42) (2022) e2203545.
[111] F. Xie et al., J. Mater. Chem. A 7 (48) (2019) 27567.
[112] H. Yamamoto et al., J. Mater. Chem. A 6 (35) (2018) 16844.
[113] Z.V. Bobyleva et al., ACS Appl. Energy Mater. 6 (1) (2022) 181.
[114] A. Beda et al., J. Mater. Chem. A 9 (3) (2021) 1743.
[115] C. Wu et al., Chem. Sci. 15 (17) (2024) 6244.
[116] M. Liu et al., Adv. Mater. 35 (29) (2023) e2300002.
[117] M. Song et al., Energy Storage Mater. 51 (2022) 620.
[118] Y.-F. Du et al., Carbon 178 (2021) 243.
[119] R. Xu et al., Carbon 206 (2023) 94.
[120] C. Fan et al., Carbon 205 (2023) 353.
[121] G. Zhang et al., ACS Appl Mater Interfaces 13 (27) (2021) 31650.
[122] X. Tang et al., Nano Res. 16 (11) (2023) 12579.
[123] H. Zhang et al., Energy Storage Mater. 73 (2024) 103796.
[124] H. Xu et al., Nano Res. 16 (8) (2023) 10985.
[125] Z. Lu et al., Proc. Natl. Acad. Sci. U.S.A. 119 (40) (2022) e2210203119.
[126] H. Lu et al., Nano Energy 64 (2019) 103903.
[127] H. He et al., Adv. Energy Mater. 13 (16) (2023) 2300357.
[128] H. Chen et al., Energy Storage Mater. 56 (2023) 532.
[129] M.H. Song et al., Nano Res. 16 (7) (2023) 9299.
[130] R. Xu et al., Battery Energy 2 (2) (2022) 20220054.
[131] X.X. He et al., ACS Appl Mater Interfaces 13 (37) (2021) 44358.
[132] W. Zhong et al., Carbon 198 (2022) 278.
[133] G. Qiu et al., Carbon 205 (2023) 310.
[134] D. Cheng et al., Carbon 182 (2021) 758.
[135] J. Zhu et al., Adv. Funct. Mater. 30 (25) (2020) 2001097.
[136] F. Yuan et al., Adv. Funct. Mater. 32 (48) (2022) 2208966.
[137] D. Sun et al., Nano Energy 64 (2019) 103937.
[138] L. Xiao et al., Adv. Energy Mater. 8 (20) (2018) 1703238.
[139] R. Guo et al., Adv. Energy Mater. 10 (9) (2020) 1903652.
[140] A. Kamiyama et al., Angew. Chem. Int. Ed. 60 (10) (2021) 5114.
[141] C. Matei Ghimbeu et al., Nano Energy 44 (2018) 327.
[142] M. Guo et al., Small (2023) e2302583.
[143] J. Li et al., Carbon 203 (2023) 469.
[144] M.P. Mercer et al., J. Mater. Chem. A 11 (12) (2023) 6543.
[145] X. Chen et al., Energy Environ. Sci. 16 (9) (2023) 4041.
[146] Y. Tong et al., Chin. Chem. Lett. 34 (1) (2023) 107443.
[147] W. Zhao et al., Small 14 (40) (2018) 1802394.
[148] Y. Li et al., Nat. Energy 9 (2) (2024) 134.
[149] Z. Guo et al., Adv. Mater. 35 (42) (2023) 2304091.
[150] Y. Zhen et al., Nano Energy 74 (2020) 104895.
[151] Y. Chen et al., J. Power Sources 557 (2023) 232534.
[152] Y. Zhen et al., Proc. Natl. Acad. Sci. u.s.a. 118 (42) (2021) 2111119118.
[153] Z. Song et al., Chem. Eng. J. 496 (2024) 154103.

Please cite this article in press as: H. Zhang et al., Materials Today, (2025), https://doi.org/10.1016/j.mattod.2025.02.014